

# *Electron Microprobe Analysis*

## Course 12.141

### Notes

**Dr. Nilanjan Chatterjee**

The electron microprobe provides a complete micrometer-scale quantitative chemical analysis of inorganic solids. The method is nondestructive and utilizes characteristic X-rays excited by an electron beam incident on a flat surface of the sample. This course provides an introduction to the theory of X-ray microanalysis through wavelength and energy dispersive spectrometry (WDS and EDS), ZAF matrix correction procedures and scanning electron imaging with back-scattered electron (BSE), secondary electron (SE), X-ray using WDS or EDS (elemental mapping), and cathodoluminescence (CL). Lab sessions involve hands-on use of the JEOL JXA-8200 Superprobe.

## MIT Electron Microprobe Facility

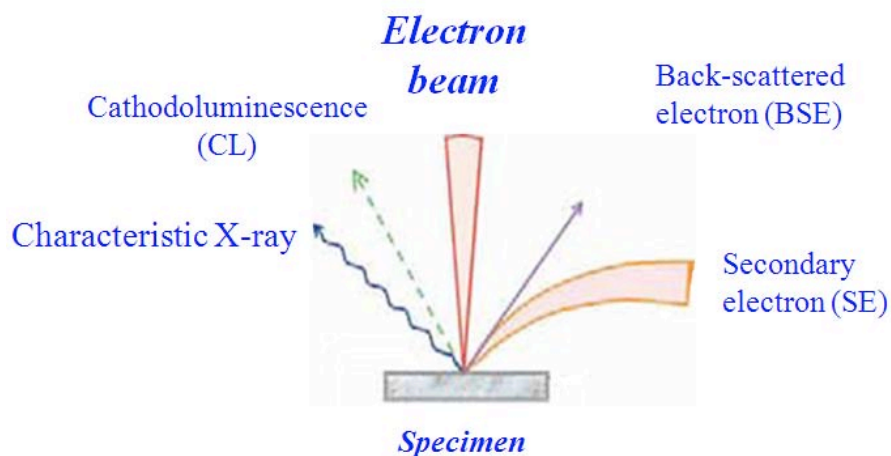
Massachusetts Institute of Technology  
Department of Earth, Atmospheric & Planetary Sciences  
web: <http://web.mit.edu/e-probe/www/>

## TABLE OF CONTENTS

	<u>Page number</u>
1. INTRODUCTION	3
2. ELECTRON SPECIMEN INTERACTIONS	5
2.1. ELASTIC SCATTERING	5
2.1.1. Electron back-scattering	5
2.1.2. Electron interaction volume	6
2.2. INELASTIC SCATTERING	7
2.2.1. Secondary electron excitation	7
2.2.2. Characteristic X-ray generation inner-shell ionization	7
2.2.3. X-ray production volume	10
2.2.4. Bremsstrahlung or Continuum X-ray generation	11
3. QUANTITATIVE X-RAY SPECTROMETRY	12
3.1. MATRIX CORRECTION	13
3.1.1. Atomic number correction (Z)	13
3.1.2. Absorption correction (A)	15
3.1.3. Characteristic fluorescence correction (F)	18
3.1.4. Continuum fluorescence correction	20
3.1.5. The $\phi(\rho z)$ correction procedure	20
4. DETECTORS IN THE ELECTRON MICROPROBE	22
4.1. ELECTRON DETECTORS	22
4.1.1. Everhart-Thornley (E-T) detector for topographic contrast	22
4.1.2. Solid-state diode detector for compositional contrast	23
4.2. CATHODOLUMINESCENCE DETECTOR	24
4.3. X-RAY DETECTORS	25
4.3.1. Energy Dispersive Spectrometer (EDS)	25
4.3.2. Wavelength Dispersive Spectrometer (WDS)	25
4.3.2.1. <i>Diffracting crystal in WDS</i>	27
4.3.2.2. <i>X-ray detector in WDS: proportional counter</i>	29
4.3.2.3. <i>Signal processing in WDS: pulse height analysis (PHA)</i>	30
5. COMPOSITIONAL IMAGING BY WDS	33
5.1. BACKGROUND CORRECTION IN WDS COMPOSITIONAL IMAGING	33
5.2. DEFOCUSING IN BEAM-RASTERED WDS X-RAY MAPS	34
6. QUANTITATIVE ANALYSIS WITH WDS	36
6.1. SAMPLE PREPARATION	36
6.2. QUALITATIVE ANALYSIS	36
6.3. CALIBRATION AND UNKNOWN ANALYSIS	37
6.3.1. Background and Peak Overlap Correction in WDS	38
7. REFERENCES	41
7.1. SOURCES AND RECOMMENDED READING	41
7.2. ACKNOWLEDGEMENTS	42

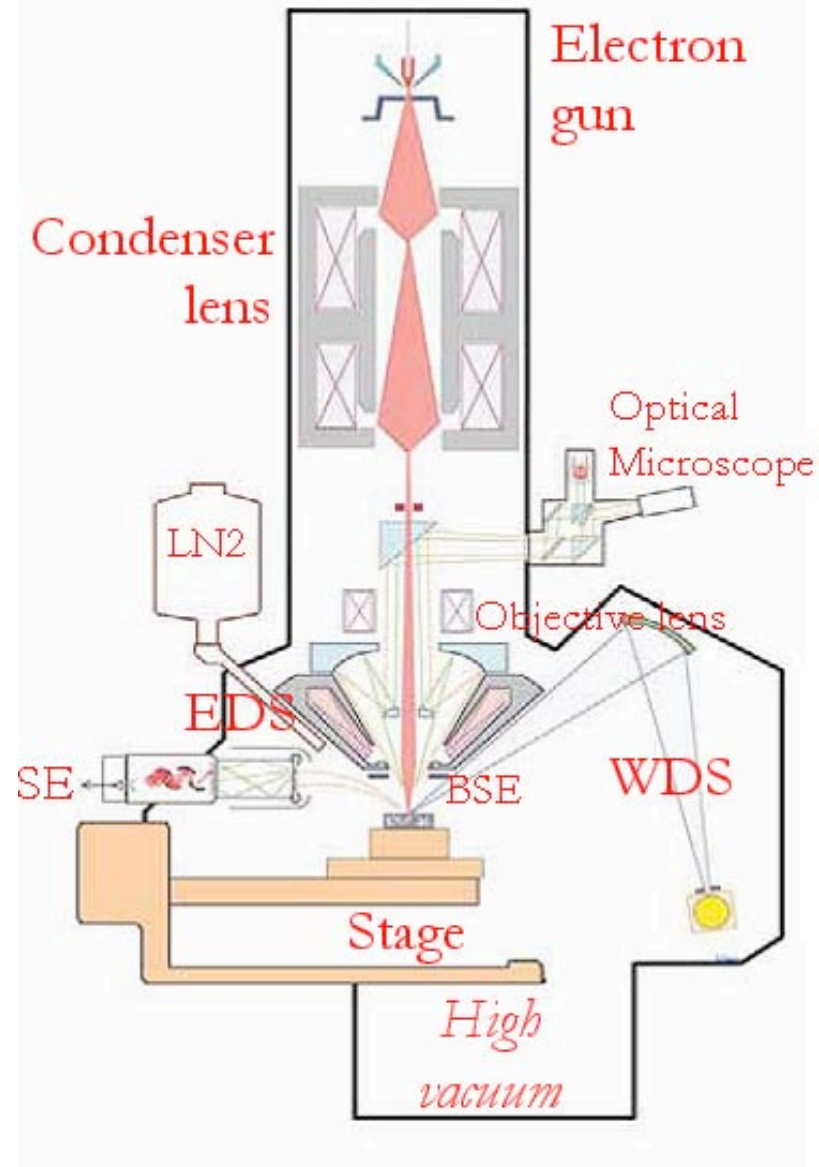
## 1. INTRODUCTION

The electron microprobe, also known as the electron probe micro-analyzer (EPMA), uses X-ray spectrometry to identify and measure concentration of elements in microscopic volumes of the specimen. In the EPMA, a finely focused electron beam interacts with the sample to generate back-scattered electrons (BSE), secondary electrons (SE), characteristic X-rays and light known as cathodoluminescence (CL). By scanning the electron beam over a surface of the sample, these signals can be used to obtain high resolution scanning electron images, X-ray maps showing spatial distribution of elements, and CL images for phase (element and compound) identification, estimation of phase distribution and proportions, trace element compositional variation and surface textural analysis of multi-phase composites. Characteristic X-rays generated from a microscopic volume in spot mode (i.e., beam not scanning) are utilized to obtain a complete quantitative chemical analysis. Sample preparation is minimal, but a well polished surface is required for accurate quantitative analysis. Although the EPMA is mostly used for studying inorganic materials, organic compounds such as polymers and biological specimens can also be studied by following special procedures and sample preparation techniques.



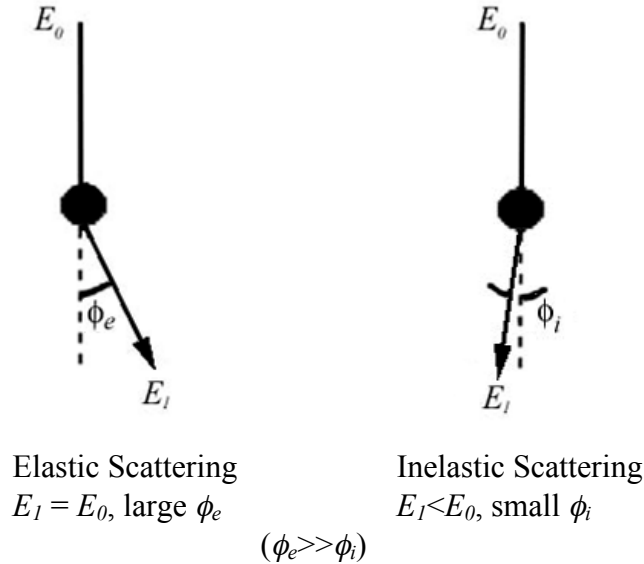
The MIT electron microprobe facility has two JEOL Superprobes: a JXA-8200 and a JXA-733. In these instruments, the electron beam is generated from a heated tungsten filament by thermionic emission in a potential difference typically between 10 and 30 kV. The JXA-8200 has an option to use a LaB<sub>6</sub> single crystal as a thermionic emission source that provides a highly stable, high intensity and smaller diameter electron beam for higher resolution imaging and more reliable chemical analysis than with the W filament. The beam is focused by two sets of coils, the condenser and the objective lenses, and several apertures that produces a final beam diameter between 1 nm and 1  $\mu\text{m}$ . Beam currents range between 1 pA and 1  $\mu\text{A}$ . A reflected light optical microscope is mounted co-axially with the electron beam for accurately setting the working distance, the distance between the sample and the objective lens. Both energy dispersive and wavelength dispersive spectrometers (EDS and WDS) are available on the microprobes for qualitative and quantitative analysis. The beam can be rastered over the sample to produce images in the magnification range of 40-360,000X. X-ray elemental maps are obtained by using the emitted X-rays as the signal source instead of BE or SE. CL images are obtained by attaching a photomultiplier to the optical microscope port on

the JXA-733. The JXA-8200 is equipped with the xClent system for high resolution, colored CL imaging and spectrometry to identify and quantify dopants and impurities in natural and synthetic semiconductors. The microprobes are maintained under high vacuum, typically in the pressure range of  $2 \times 10^{-5}$ - $10^{-6}$  torr (about one-billionth of the atmospheric pressure), by a combination of mechanical and diffusion pumps.



## 2. ELECTRON SPECIMEN INTERACTIONS

When an electron beam strikes a target (that is, the sample), the electrons are scattered by the target atoms. There are two types of electron scattering:



where,  $E_0$  is the energy of the incident electron;  $E_1$ , the energy of the electron after scattering;  $\phi_e$ , the elastic scattering angle; and  $\phi_i$ , the inelastic scattering angle.

### 2.1. ELASTIC SCATTERING

Elastic scattering affects trajectories of the beam electrons inside the specimen without significantly altering the kinetic energy of the electron (e.g., electron back-scattering). The scattering probability or **cross-section** of elastic scattering,  $Q$  for scattering angles greater than  $\phi_e$ , is given by the screened Rutherford expression:

$$Q(>\phi_e) = 1.62 \times 10^{-20} (Z^2/E^2) \cot^2(\phi_e/2) \quad (2.1)$$

events.cm<sup>2</sup>/e<sup>-</sup>.atom; where,  $Z$  is the atomic number; and  $E$ , the incident electron energy (keV).  $Q$  is thus proportional to the square of  $Z$  of the target, and inversely proportional to the square of  $E$  of the electron beam.

#### 2.1.1. Electron back-scattering

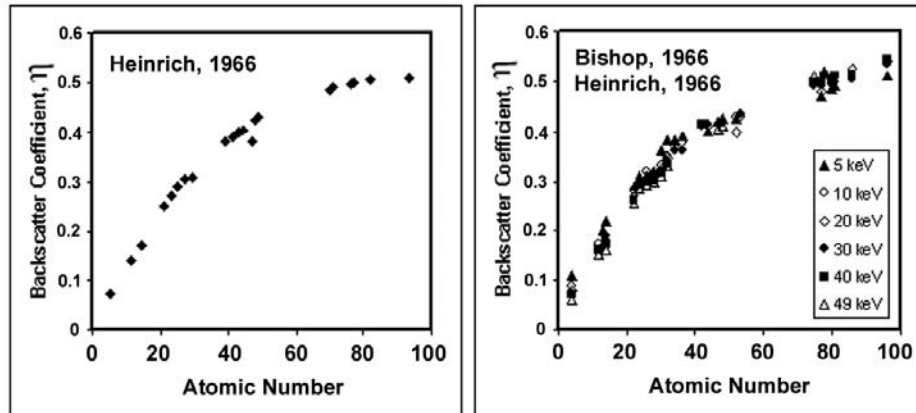
When the elastic scattering angle is greater than 90°, backscattering occurs. It may also occur through multiple scattering at high angles. The **back-scatter coefficient**,  $\eta$ , is the fraction of beam electrons scattered backward:

$$\eta = n_{\text{BSE}}/n_{\text{B}} = i_{\text{BSE}}/i_{\text{B}} \quad (2.2)$$

where,  $n_B$  is the number of incident beam electrons and  $n_{BSE}$  is the number of back-scattered electrons ( $i$ 's denote current). For compounds,  $\eta$  is given as:

$$\eta = \sum_j C_j \eta_j \quad (2.3)$$

where,  $j$  denotes the constituent elements and  $C_j$  the concentration  $j$  in the compound.  $\eta$  increases monotonically with atomic number and it is independent of beam energies above 5 keV.

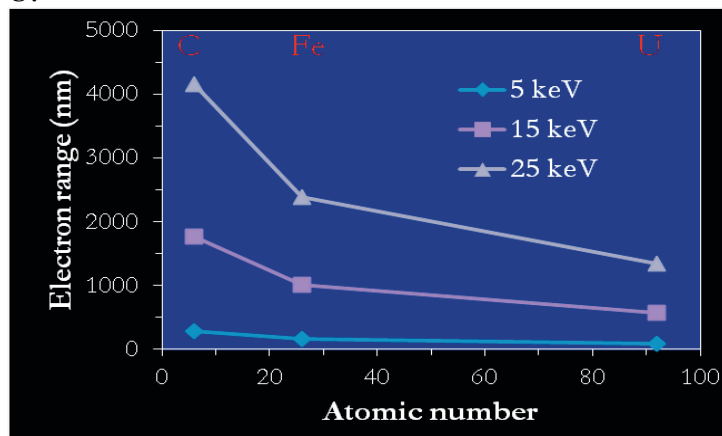


### 2.1.2. Electron interaction volume

The electron range is the distance between the point where the beam electrons enter the specimen and the point where they lose all their energy and leave the specimen as sample current. The *Kanaya-Okayama range* takes into the account the combined effects of elastic and inelastic scattering and is given by:

$$R_{KO} = KE_0^n / \rho \quad (2.4)$$

( $\mu\text{m}$ ), where,  $K = 0.0276A/Z^{0.889}$ ,  $A$  (g/mole), the atomic weight,  $Z$ , the atomic number,  $\rho$  ( $\text{g}/\text{cm}^3$ ), the density,  $E_0$  (keV), the incident beam energy, and  $n = 1.67$ . Typical ranges (at perpendicular beam incidence and 15 keV beam energy) are 1.8  $\mu\text{m}$  for C, 1.1  $\mu\text{m}$  for Fe and 0.8  $\mu\text{m}$  for U.



*Monte Carlo electron-trajectory simulations* have shown that the size of the electron interaction volume in a specimen increases with the incident beam energy. There is less elastic scattering as beam energy increases (Eqn. 2.1) and the electrons are able to penetrate deeper into the specimen at higher beam energies. The interaction volume decreases with increasing atomic number as predicted by Eqn. 2.1. Experiments suggest that the interaction volume has a distinct pear shape for low atomic number targets, whereas, it becomes spherical for larger atomic number targets. Most of the back-scattered electrons come from the top part of the interaction volume. For example, 90% of the back-scattering occurs in the top 17% of the depth of electron penetration in Au and the top 29% of the depth in C (at perpendicular beam incidence and 20 keV beam energy).

## 2.2. INELASTIC SCATTERING

Inelastic scattering involves transfer of energy from the beam electrons to the atoms of the specimen (e.g., generation of secondary electrons, Auger electrons, characteristic X-rays and bremsstrahlung or continuum X-rays). The trajectory of the beam electron is not altered significantly.

### 2.2.1. Secondary electron excitation

Some sample electrons mobilized through inelastic scattering by beam electrons overcome the surface energy barrier and escape from the sample. These electrons are known as *secondary electrons*. They have lower energies (<50 eV; majority <10 eV) compared to back-scattered electrons.

The *secondary electron coefficient*,  $\delta$ , is defined as

$$\delta = n_{SE}/n_B = i_{SE}/i_B \quad (2.5)$$

where,  $n_B$  is the number of incident beam electrons and  $n_{SE}$  is the number of secondary electrons ( $i$ 's denote current). Compared to the backscatter coefficient,  $\delta$  is relatively insensitive to the target atomic number. It generally increases with a decrease in the beam energy.

Although sample electrons are mobilized throughout the interaction volume, their escape probability from the surface of the sample decreases sharply with depth. The *escape depth of secondary electrons is only about 1/100 of that for backscattered electrons* for incident beam energies in the range 10-30 keV. Hence, secondary electrons are useful in studying the surface characteristics of the sample. Samples are commonly coated with a thin film of gold that enhances the secondary electron yield.

### 2.2.2. Characteristic X-ray generation: inner-shell ionization

X-rays are electromagnetic radiations in the energy range of about 0.12 to 120 keV (wavelength range: of 10 to  $10^{-2}$  nanometer). The typical range of X-ray energies analyzed in the EPMA are between 0.12 and 10 keV. An element is identified by its characteristic set of emitted X-ray energies.

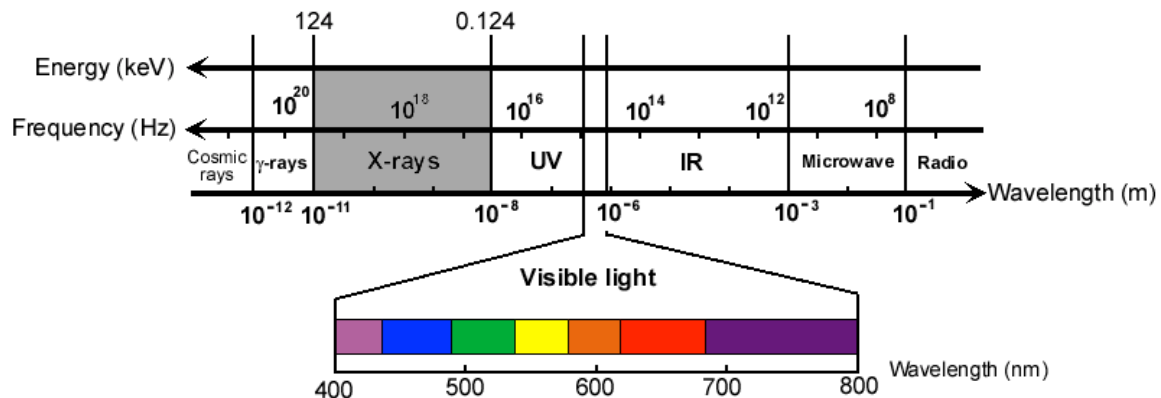
The **energy,  $E$** , of an X-ray is given by

$$E = h\nu \quad (2.6)$$

Where,  $h$  is the Planck's constant ( $6.626 \times 10^{-34}$  Joule.sec =  $6.626 \times 10^{-34} / 1.6021 \times 10^{-16}$  keV.sec) and the frequency  $\nu = c/\lambda$ ,  $c$  being the speed of light in vacuum ( $2.99793 \times 10^{17}$  nm/sec) and  $\lambda$  being the **wavelength**. Thus, the wavelength is related to the energy as:

$$\lambda = hc/E = 1.2398/E \quad (2.7)$$

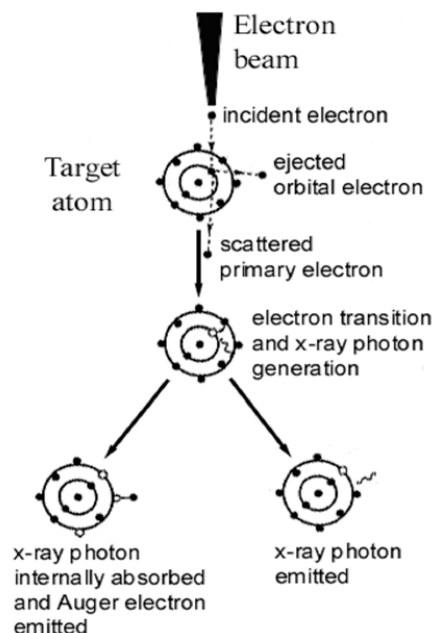
where,  $\lambda$  is in nm and  $E$  is in keV.



When the beam electrons scatter inelastically, tightly bound inner shell electrons may be ejected from the target atoms if the beam energy is higher than the **critical excitation energy,  $E_c$**  (also known as **X-ray absorption edge energy**), of the target atomic shell. The **overvoltage,  $U$** , of the electron beam, expressed as:

$$U = E/E_c \quad (2.8)$$

where,  $E$  is the beam energy, must be greater than unity for ionization to occur.



The energy of the beam electron is diminished by an amount equal to  $E_c$  and subsequent relaxation of the target atom from its excited state involving the transfer of an outer shell electron to the ionized inner shell, results in the generation of a characteristic X-ray. This X-ray may be emitted from the atom, or it may be internally absorbed while ejecting another outer shell electron (an Auger electron). The fraction of X-rays emitted (**characteristic X-ray yield** or **fluorescent yield,  $\omega$** ) for a specific shell increases with the atomic number, whereas the **Auger yield,  $\alpha$** , decreases.

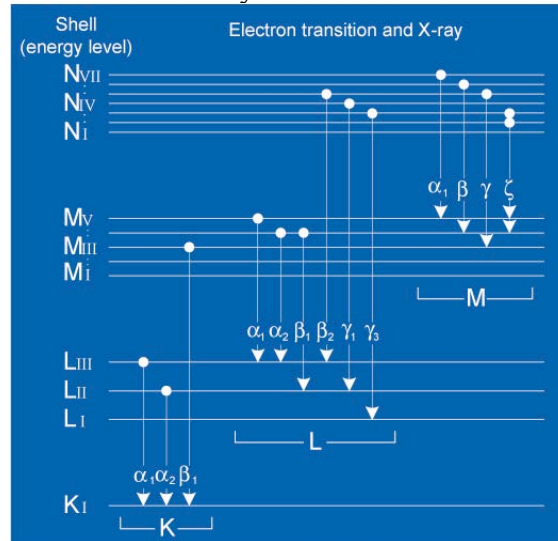
Characteristic X-rays are named as follows:

$K\alpha$ : when vacancy in K-shell is filled by a transition from L-shell,

$K\beta$ : when vacancy in K-shell is filled by a transition from M-shell,

$L\alpha$ : when vacancy in L-shell is filled by a transition from M-shell,

$M\alpha$ : when vacancy in M-shell is filled by a transition from N-shell, etc.



The **cross-section of inner shell ionization** is given by Bethe as follows:

$$Q = 6.51 \times 10^{-20} [(n_s b_s) / (U E_c^2)] \ln(c_s U) \quad (2.9)$$

ionizations.cm<sup>2</sup>/e<sup>-</sup>.atom), where  $n_s$  is the number of electrons in a shell or subshell (e.g.,  $n_s=2$  for a K shell),  $b_s$  and  $c_s$  are constants for a particular shell,  $E_c$  (keV) is the critical excitation energy of the shell, and  $U$  is the overvoltage. For the K-shell, the constants are  $b_s=0.3$  and  $c_s=1$  at  $U<4$ , and  $b_s=0.9$  and  $c_s=0.65$  at  $4<U<25$ .

Energy lost by the beam electrons due to inelastic scatterings is given by Bethe as:

$$dE/ds = -7.85 \times 10^4 (Z\rho/AE_m) \ln(1.166E_m/J) \quad (2.10)$$

where, the constant is equal to  $2\pi e^4 N_0$ ;  $e$  being the electronic charge and  $N_0$ , the Avogadro's number;  $Z$  is the atomic number;  $A$  (g/mole), the atomic weight,  $\rho$  (g/cm<sup>3</sup>), the density,  $E_m$  (keV), the average energy along path segment  $s$ , and  $J$ , the mean ionization potential given by Berger & Seltzer:

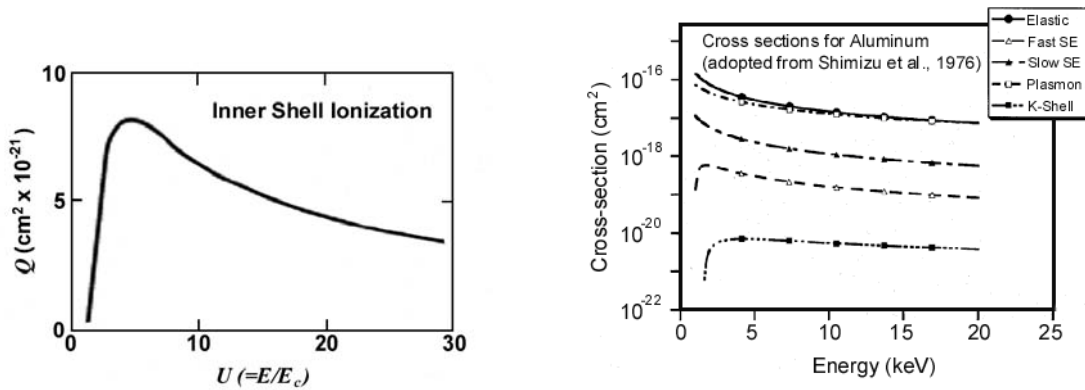
$$J \text{ (keV)} = (9.76Z + 58.82 Z^{0.19}) \times 10^{-3} \quad (2.11)$$

The **electron stopping power** of a material,  $S$ , is a function of its density and rate of energy loss of the beam electrons (Eqn. 2.10). It is defined by the following expression:

$$S = -(1/\rho)(dE/ds) \quad (2.12)$$

where,  $\rho$  is the density and  $dE/ds$ , the rate of electron energy loss with distance.

The cross-section of inner-shell ionization is maximum at overvoltage values between 3 and 5. Cross-sections of all types of inelastic scattering decrease with increasing incident beam energy.



### 2.2.3. X-ray production volume

Since characteristic X-rays are produced only when the incident beam energy exceeds  $E_c$ , the X-ray range is always smaller than the electron range. The **X-ray range** according to Anderson & Hassler is:

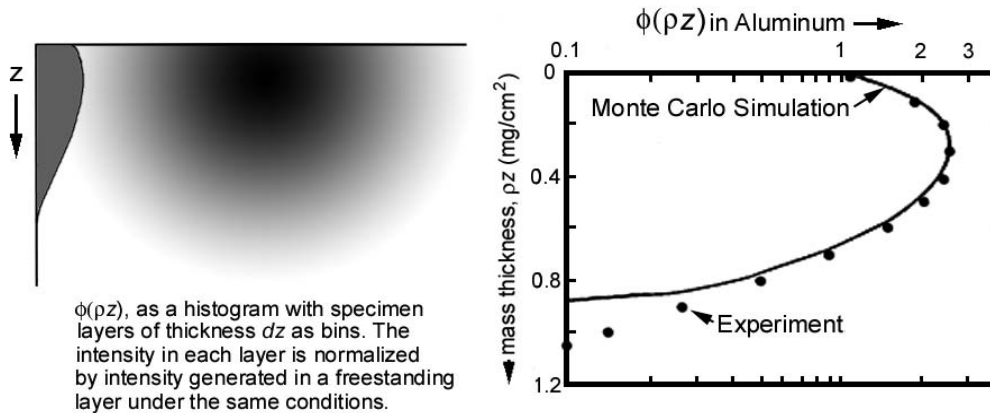
$$R = K(E_0^n - E_c^n)/\rho \quad (2.13)$$

( $\mu\text{m}$ ) where,  $K = 0.064$ , and  $n = 1.68$ . The range of primary X-ray generation is critical in estimating the sampling volume in X-ray microanalysis.

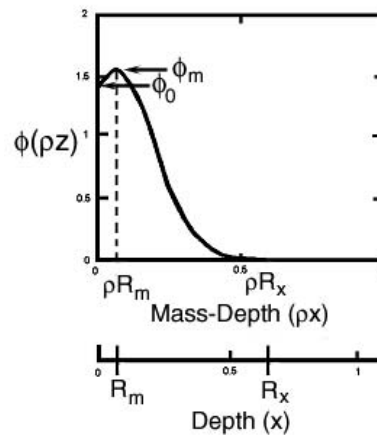
The distribution of X-ray generation sites within the interaction volume is given by the **depth-distribution function**,  $\phi(\rho z)$ , which is a histogram showing the number of X-rays generated in layers of the specimen, each with a thickness of  $dz$ , relative to the number of X-rays the beam would produce in a freestanding layer of the same material of thickness  $dz$ .

$$I_{\text{generated}} = \phi(\Delta\rho z) \int_0^\infty \phi(\rho z) d(\rho z) \quad (2.14)$$

where,  $\phi(\Delta\rho z)$  is the intensity generated in a freestanding layer of thickness  $\Delta\rho z$ . The upper layers produce more X-rays than a freestanding layer because the incident electrons travel randomly between layers by multiple scattering. With increasing depth, however, the electrons lose their energy and finally, their ability to ionize inner-shells as the instantaneous overvoltage drops below unity.



Value of  $\phi(\rho z)$  at the surface,  $\phi_0$ ; the maximum value of  $\phi(\rho z)$ ,  $\phi_m$ ; the depth at  $\phi_m$ ,  $R_m$ ; and the maximum depth where  $\phi(\rho z)$  is zero,  $R_x$  are the parameters used to describe a  $\phi(\rho z)$  distribution. Both  $R_m$  and  $R_x$  decrease with atomic number ( $Z$ ) and increase with beam energy ( $E_0$ ).  $\phi_0$  increases with  $E_0$ .



#### 2.2.4. Bremsstrahlung or Continuum X-ray generation

As the beam electrons approach the target atoms, some of the electrons lose a part or all of their energy by deceleration in the Coulombic field created by the outer shell electrons of the target atom. The energy lost by the beam electron is converted into bremsstrahlung or continuum X-rays with maximum energies up to the total initial energy of the beam electron. The maximum continuum X-ray energy, known as the Duane-Hunt limit, provides a means for accurately measuring the energy of the electron beam.

### 3. QUANTITATIVE X-RAY SPECTROMETRY

The *primary generated* characteristic X-ray intensities are roughly proportional to the respective mass-fractions of the emitting elements.

$$C_i \propto I_i \quad (3.1)$$

where,  $C_i$  and  $I_i$  are the weight concentration and primary generated X-ray intensity of element  $i$ . In quantitative analysis, the intensity is compared against the intensity of the same element generated from a standard,  $I_{(i)}$ , with a known concentration  $C_{(i)}$  of that element. The ratio of the intensity from the sample and standard is known as the ***k-ratio***.

$$\frac{C_i}{C_{(i)}} \propto \frac{I_i}{I_{(i)}} \quad (3.2)$$

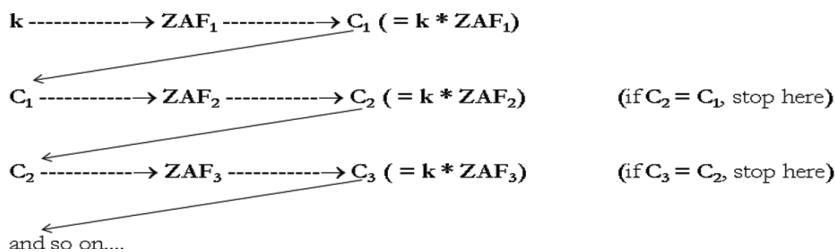
where,

$$\frac{I_i}{I_{(i)}} = k_i \quad (3.3)$$

Because of interaction of the primary generated X-rays with the specimen atoms, the emitted X-rays have a different intensity from the generated intensity. This matrix effect is taken into account by modifying the above equation as:

$$\frac{C_i}{C_{(i)}} = k_i \cdot [\text{ZAF}]_i \quad (3.4)$$

where,  $[\text{ZAF}]_i$  is the ***matrix correction factor*** for element  $i$ . However, the matrix correction depends on the composition of the specimen. Since the composition is unknown before the analysis, the ZAF factors are also unknown. Therefore, the concentration  $C_i$  is determined through iteration. The measured k-ratios ( $k_i$ ) are used as a first estimate of the concentrations and the ZAF factors are calculated. The concentrations ( $C_i$ ) are then calculated by multiplying the k-ratios with the corresponding ZAF factors calculated in the last step. A new set of ZAF factors are then calculated using the  $C_i$  values obtained in the last step, and concentrations are recalculated by multiplying the ZAF's with the original k-ratios. The process is repeated until the calculated  $C_i$  does not change from the previous step. The following flow-chart demonstrates the procedure:



### 3.1. MATRIX CORRECTION

The atomic number correction,  $\mathbf{Z}$ , the absorption correction,  $\mathbf{A}$ , and the fluorescence correction,  $\mathbf{F}$  are the three constituents of the matrix correction.

#### 3.1.1. Atomic number correction ( $\mathbf{Z}$ )

The atomic number correction depends on the average atomic numbers of the specimen and the standard. It is a function of the electron back-scattering factor ( $R$ ) and the electron stopping power ( $S$ , Eqn. 2.12).  $R$  is the ratio of number of X-rays actually generated to number of X-rays generated if there were no backscatter.

The atomic number correction  $\mathbf{Z}_i$  for element  $i$  is given by Duncumb & Reed (1968) as:

$$\mathbf{Z}_i = \frac{R_i \int_{E_c}^{E_0} \frac{Q}{S} dE}{R_i^* \int_{E_c}^{E_0} \frac{Q}{S^*} dE} \quad (3.5)$$

where,  $Q$  is the ionization cross-section (Eqn. 2.9), and  $R$  and  $S$  marked by \* are for the specimen (unmarked  $R$  and  $S$  are for the standard). The back-scattering factor,  $R_i$ , varies both with the atomic number and the overvoltage ( $U$ ). As the overvoltage decreases toward unity, fewer electrons with energies greater than  $E_c$  are back-scattered and hence, more electrons are available to cause ionization.  $R_i$  is expressed as:

$$R_i = \sum_j C_j R_{ij} \quad (3.6)$$

where,  $j$  represents the elements present in the standard or the specimen. Yakowitz et al. (1973) express  $R_{ij}$  as:

$$R_{ij} = R'_1 - R'_2 \ln(R'_3 Z_j + 25) \quad (3.7)$$

where,

$$R'_1 = 8.73 \times 10^{-3} U^3 - 0.1669 U^2 + 0.9662 U + 0.4523 \quad (3.8)$$

$$R'_2 = 2.703 \times 10^{-3} U^3 - 5.182 \times 10^{-2} U^2 + 0.302 U - 0.1836 \quad (3.9)$$

$$R'_3 = (0.887 U^3 - 3.44 U^2 + 9.33 U - 6.43) / U^3 \quad (3.10)$$

The stopping power,  $S_i$ , is expressed as:

$$S_i = \sum_j C_j S_{ij} \quad (3.11)$$

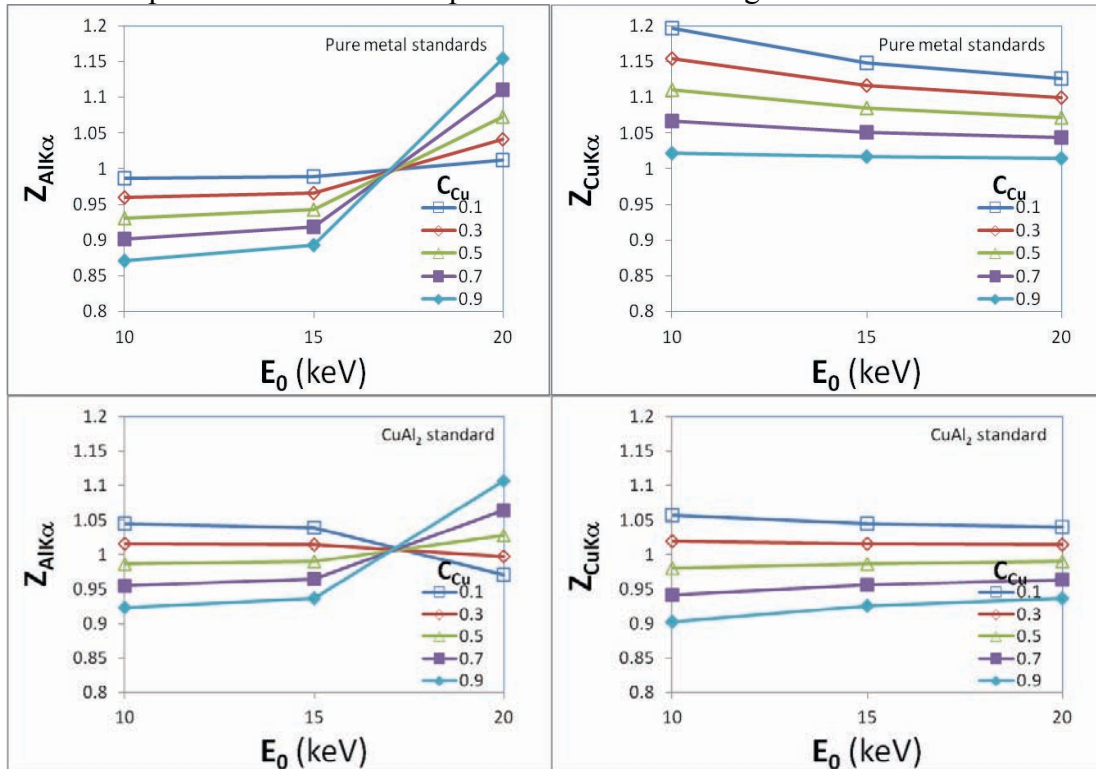
where,  $j$  represents the elements present in the standard or the specimen. Thomas (1964) approximates the mean energy  $E_m$  (Eqn. 2.10) as  $(E_0 + E_c)/2$ .  $S_{ij}$  then becomes:

$$S_{ij} = (\text{const}) [(2Z_j/A_j)/(E_0+E_c)] \ln[583(E_0+E_c)/J_j] \quad (3.12)$$

$Q$  is assumed to be constant and cancels out in the expression for  $Z_j$ . The constant in Eqn. 3.12 also cancels out. Further, avoiding the integration in Eqn. 3.5,  $Z_j$  can be approximately expressed as:

$$Z_j = (R_i S_i^*) / (R_i^* S_i) \quad (3.13)$$

To demonstrate the effect of the atomic number difference between the specimen and the standard, the atomic number correction is calculated with the above equations for a complete range of Cu-Al alloys with respect to metal standards ( $Z_{Al}=13$ ,  $Z_{Cu}=29$ ) and a  $\theta$ -phase ( $\text{CuAl}_2$ ; average atomic number,  $Z=21.6$ ) standard. There is a large atomic number difference for Cu between the specimen and the Cu standard in the  $\text{Cu}_{10\text{wt\%}}\text{Al}_{90\text{wt\%}}$  alloy ( $C_{Cu}=0.1$ ;  $Z=14.6$ ). Hence, the atomic number correction for  $\text{CuK}\alpha$  is also large ( $Z_{\text{CuK}\alpha} = 1.149$  at  $E_0=15$  keV). The atomic number difference is small for Al in the same alloy. So, the correction for  $\text{AlK}\alpha$  ( $Z_{\text{AlK}\alpha} = 0.989$  at  $E_0=15$  keV) is also small. When the  $\theta$ -phase is used as a standard for the same alloy, the atomic number difference for Cu decreases, whereas, it increases for Al. As a result,  $Z_{\text{CuK}\alpha}$  decreases to 1.045 (a decrease of  $\sim 60\%$ ) and  $Z_{\text{AlK}\alpha}$  increases to 1.038 under the same beam energy condition. An important conclusion from these graphs is that it is preferable to choose a standard with a composition similar to the specimen so that the magnitude of  $Z$  is small.

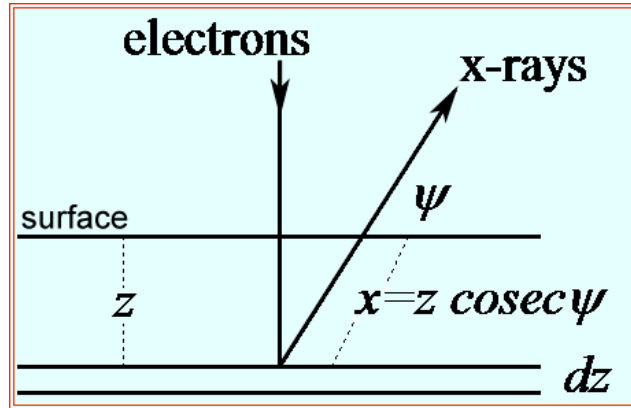


The crossover at  $\sim 17$  keV of the  $Z_{\text{AlK}\alpha}$  values in the one of the graphs may be an artifact of the complex polynomial fit of the Duncumb & Reed data by Yakowitz et al.. Yakowitz's equations probably fail to work above a certain value of  $U$ ,  $U_{Al}=9.62$  (corresponding to  $E_0=15$  keV) in this case. The relation between  $Z_j$  and  $U$  is complex,

although in general,  $Z_i$  decreases very slowly with an increase in  $U$ . The uncertainty in  $Z_i$  does not change much as  $U$  increases. Since, as we will see later, high  $U$  values require large absorption corrections, a low  $U$  is preferable.

### 3.1.2. Absorption correction (A)

Not all the primary generated X-rays are emitted from the specimen. Some of the X-rays generated at depth are absorbed in the specimen by interacting with other specimen atoms, which may become ionized as a result. The emitted intensity of element  $i$  is given as:



$$I_{i(\text{emitted})} = I_{i(\text{generated})} \exp\left(-\left(\frac{\mu}{\rho}\right)_{\text{specimen}}^{i\text{-energy}} (\rho x)\right) \quad (3.14)$$

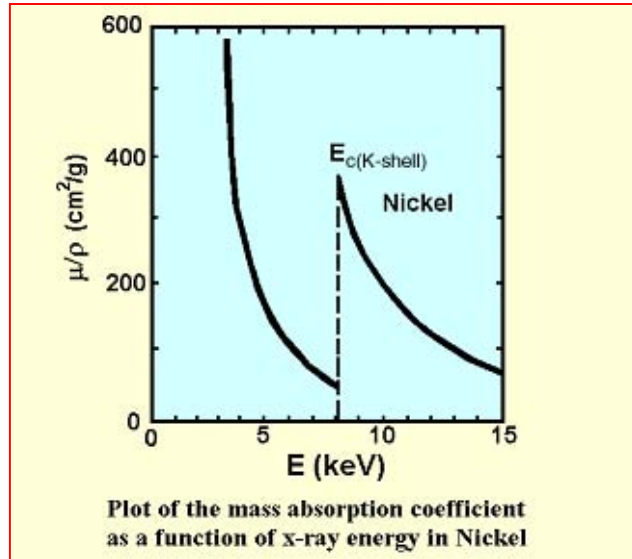
where,

$$x = z \operatorname{cosec} \psi \quad (3.15)$$

is the distance traveled by the X-ray inside the sample along an angle  $\psi$  (angle measured from the sample surface, also known as the *take-off angle*),  $z$  is the depth and the electron beam is perpendicular to the surface of the sample.  $\left(\frac{\mu}{\rho}\right)_{\text{specimen}}^{i\text{-energy}}$  is known as the **mass absorption coefficient** ( $\text{cm}^2/\text{g}$ ) of the specimen for the particular X-ray energy of element  $i$ .

The  $\left(\frac{\mu}{\rho}\right)_{\text{specimen}}^{i\text{-energy}}$  of the specimen decreases with increasing incident X-ray energy, until the incident energy is slightly higher than an absorption edge (or critical excitation energy) of an element present in the specimen, where  $\left(\frac{\mu}{\rho}\right)_{\text{specimen}}^{i\text{-energy}}$  jumps to a high value.

This means that absorption is maximum when the energy of the X-ray is slightly above the critical excitation energy of the target atomic shell concerned. In the following example,  $\text{ZnK}\alpha$  is absorbed by Ni because the energy of  $\text{ZnK}\alpha$  (8.632 keV) is slightly higher than the critical excitation energy of the K-shell of Ni ( $E_c = 8.331$  keV).



Energy (keV)	$E_{c(K-shell)}$ (keV)	$(\mu/\rho)_{Ni}^{energy}$ (cm <sup>2</sup> /g)
CoK $\alpha$ 6.925		53
<b>NiK<math>\alpha</math> 7.472</b>	<b><u>8.331</u></b>	60
<b>CuK<math>\alpha</math> 8.041</b>		<b>49</b>
<b>ZnK<math>\alpha</math> 8.632</b>		<b><u>311</u></b>

The total X-ray intensity emitted from an infinitesimal layer  $d(\rho z)$  at a depth  $z$  can be expressed in terms of the depth-distribution function  $\phi(\rho z)$  as:

$$dI'_i = \phi_i(\rho z) \exp\left(-\left(\frac{\mu}{\rho}\right)_{specimen}^{i-energy} (\rho z \operatorname{cosec} \psi)\right) d(\rho z) \quad (3.16)$$

where,  $\phi_i(\rho z)d(\rho z)$  is the intensity of x-ray generated in the layer  $d(\rho z)$ . The total emitted intensity thus becomes,

$$I_{i(emitted)} = \phi_i(\Delta\rho z) \int_0^{\infty} \phi_i(\rho z) \exp^{-\chi_i \rho z} d(\rho z) \quad (3.17)$$

where,

$$\chi_i = \left(\frac{\mu}{\rho}\right)_{specimen}^{i-energy} \operatorname{cosec} \psi \quad (3.18)$$

The *absorption function*,  $f(\chi_i)$ , defined as the emitted fraction of the generated intensity,  $I_{i(emitted)}/I_{i(generated)}$ , is given by,

$$f(\chi_i) = \frac{\int_0^{\infty} \phi_i(\rho z) \exp^{-\chi_i \rho z} d(\rho z)}{\int_0^{\infty} \phi_i(\rho z) d(\rho z)} \quad (3.19)$$

The absorption correction  $A_i$  for an element  $i$  in a compound is given by:

$$\mathbf{A}_i = \frac{f(\chi_i)}{f(\chi_i)^*} \quad (3.20)$$

where, the specimen is noted by \*. Philibert (1963) modeled the absorption function  $f(\chi_i)$  semi-empirically as:

$$f(\chi_i) = \left[ \left( 1 + \frac{\chi_i}{\sigma_i} \right) \left( 1 + \frac{\chi_i}{\sigma_i} \frac{h_i}{1 + h_i} \right) \right]^{-1} \quad (3.21)$$

where,

$$h_i = 1.2A_i/Z_i^2 \quad (3.22)$$

and

$$\sigma_i = 4.5 \times 10^5 / (E_0^{1.65} - E_{i(c)}^{1.65}) \quad (3.23)$$

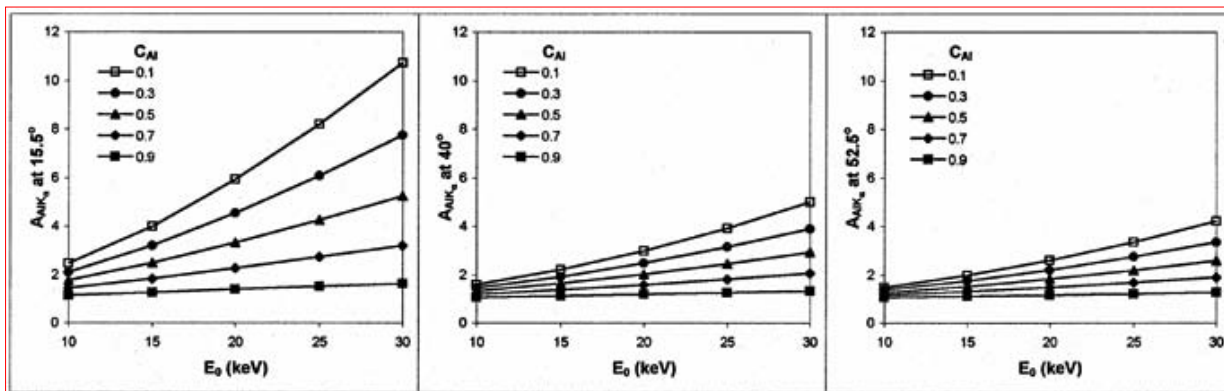
$\sigma$ , which takes into account the accelerating voltage and the critical excitation energy, is known as the Lenard coefficient and its formulation is given by Duncumb & Shields (1966) and Heinrich (1969). For compounds, the value of  $h$ , and  $(\mu/\rho)_{specimen}^{i-energy}$  are evaluated as follows:

$$h_i = \sum_j h_j C_j \quad (3.24)$$

$$(\mu/\rho)_{specimen}^{i-energy} = \sum_j (\mu/\rho)_{element\ j}^{i-energy} C_j \quad (3.25)$$

Philibert obtained his equation by empirically fitting  $\phi(\rho z)$  function of elements available at that time, but simplified the fit by setting  $\phi_0=0$  (the value of  $\phi(\rho z)$  at the surface). However,  $\phi_0$  is always  $>1$  due to scattering of back-scattered electrons within the sample. Hence, in cases where most of the X-rays are generated near the surface (e.g., light element (C,N,O) X-rays in a metal matrix (Ti,Fe,Cu)), the Philibert equation produces erroneous results.

The absorption correction is a function of the mass absorption coefficients, the take-off angle and the accelerating voltage. To understand the effect of these three parameters on the absorption correction, the Mg-Al binary alloy is considered.  $\text{AlK}\alpha$  ( $E_K=1.487$  keV) is highly absorbed in Mg ( $E_{c(K-shell)}=1.303$  keV) with  $(\mu/\rho)_{Mg}^{\text{AlK}\alpha} = 4168$   $\text{cm}^2/\text{g}$ . The following plots show calculated absorption corrections for  $\text{AlK}\alpha$  (using  $E_c$  from Bearden, 1964 and  $(\mu/\rho)$  from Heinrich, 1986) for different compositions of the Mg-Al alloy under different  $E_0$  and  $\psi$  conditions. Three conclusions emerge from these plots: the absorption correction,  $\mathbf{A}_{\text{AlK}\alpha}$ , increases with increasing operating voltage, decreasing take-off angle and increasing Mg in the specimen. Shorter distances traveled by a primary X-ray within the sample lessens its absorption. Therefore, higher take-off angles and lower operating voltages lead to a lower absorption correction. Also, more Mg in the sample leads to a more efficient absorption of the  $\text{AlK}\alpha$ . Most electron microprobes have fixed take-off angles. Hence, a low overvoltage should be used to minimize the absorption correction.



The error in the mass absorption coefficient propagates into the final result. The effect of uncertainties in mass absorption coefficients is low when the value of the absorption function  $f(\chi)$  is greater than 0.7.

### 3.1.3. Characteristic fluorescence correction (F)

X-ray fluorescence occurs as a consequence of photoelectric absorption of primary X-rays as the target atom relaxes from an excited state. These secondary X-rays may be generated both by characteristic or continuum x-rays. Since X-rays can travel longer distances than electrons in matter, the *range of fluoresced X-rays is also greater (~10 times) than the primary electron interaction range*. The secondary X-ray interaction volume may be as much as 1000 times greater than the primary interaction volume.

Element (Atomic No.)	$E_{K\alpha}$ (keV)	$E_{K\beta}$ (keV)	$E_{c(K-shell)}$ (keV)	$\left(\frac{\mu}{\rho}\right)_{\text{absorber}}^{NiK\alpha}$ (cm <sup>2</sup> /g)
Mn(25)	5.895	6.492	<u>6.537</u>	<u>344</u>
Fe(26)	6.4	7.059	<u>7.111</u>	<u>380</u>
Co(27)	6.925	7.649	7.709	53
Ni(28)	<u>7.472</u>	8.265	<u>8.331</u>	59
Cu(29)	8.041	<u>8.907</u>	8.98	65.5

The data in the above table indicates that NiK $\alpha$ , with an energy of 7.472 keV, will be efficiently absorbed in Fe and Mn, whose K-shell critical excitation energies are 7.111 keV and 6.537 keV, respectively. As a result, both Fe and Mn (K $\alpha$  and K $\beta$ ) will be fluoresced by NiK $\alpha$ . The table also shows that NiK $\alpha$  and K $\beta$  can only be fluoresced by CuK $\beta$  because only CuK $\beta$  has an energy (8.907 keV) greater than the Ni K-shell absorption edge (8.331 keV). CuK $\beta$  will be absorbed in the process. The following table shows which X-rays will cause fluorescence in the different elements:

Element	Radiation causing fluorescence
Mn	FeK $\beta$ , CoK $\alpha$ , CoK $\beta$ , NiK $\alpha$ , NiK $\beta$ , CuK $\alpha$ , CuK $\beta$
Fe	CoK $\beta$ , NiK $\alpha$ , NiK $\beta$ , CuK $\alpha$ , CuK $\beta$
Co	NiK $\beta$ , CuK $\alpha$ , CuK $\beta$
Ni	CuK $\beta$
Cu	none

The fluorescence correction for element  $i$  in a compound of  $j$  elements is as follows:

$$F_i = \frac{\left(1 + \sum_j \left\{ I_{ij}^f / I_i \right\}\right)}{\left(1 + \sum_j \left\{ I_{ij}^f / I_i \right\}\right)^*} \quad (3.26)$$

where,  $I_{ij}^f$  is the intensity of element  $i$  fluoresced by element  $j$ , and  $I_i$  is the primary X-ray intensity produced by the electron beam. For an elemental standard, the numerator reduces to unity.  $I_{ij}^f / I_i$  is given by Castaing (1951) and modified by Reed (1965) as:

$$I_{ij}^f / I_i = C_j Y_0 Y_1 Y_2 Y_3 P_{ij} \quad (3.27)$$

where,

$$Y_0 = 0.5[(r_i-1)/r_i][\omega_j A_i / A_j] \quad (3.28)$$

where,  $r_i$  is the absorption edge jump-ratio;  $(r_i-1)/r_i$  is 0.88 for K-line, 0.75 for L-line; and  $\omega_j$  is the fluorescent yield,

$$Y_1 = [(U_j-1)/(U_i-1)]^{1.67} \quad (3.29)$$

$$Y_2 = (\mu/\rho)_i^j / (\mu/\rho)_{\text{spec}}^j \quad (3.30)$$

where,  $(\mu/\rho)_i^j$  is the mass absorption coefficient of element  $i$  for X-rays from element  $j$ ; and  $(\mu/\rho)_{\text{spec}}^j$  is the mass absorption coefficient of the specimen for X-rays from element  $j$ ,

$$Y_3 = [\ln(1+u)]/u + [\ln(1+v)]/v \quad (3.31)$$

where,

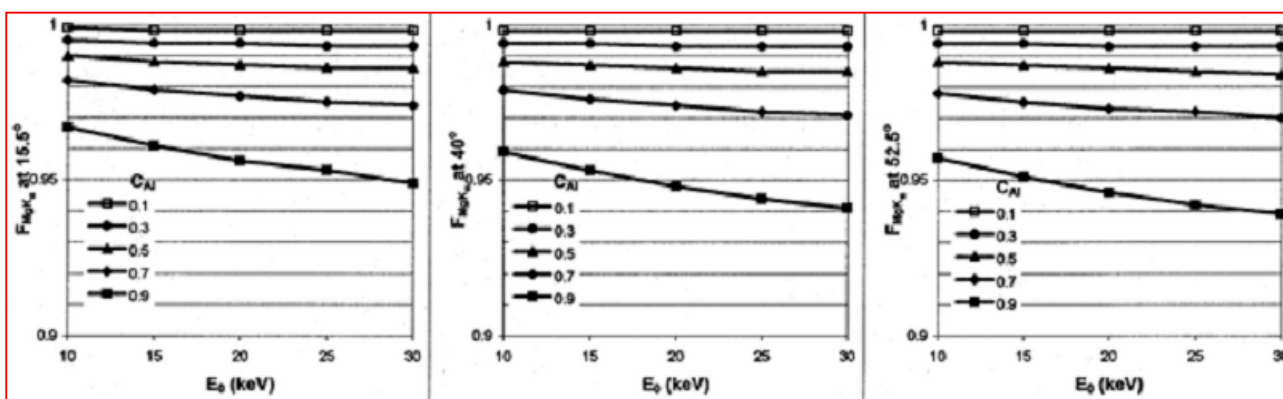
$$u = [(\mu/\rho)_{\text{spec}}^i / (\mu/\rho)_{\text{spec}}^j] \text{ cosec } \psi \quad (3.32)$$

and

$$v = 3.3 \times 10^5 / [(E_0^{1.65} - E_c^{1.65}) (\mu/\rho)_{\text{spec}}^j] \quad (3.33)$$

and,  $P_{ij}$  is a factor for the type of fluorescence occurring. For K X-ray fluorescing another K X-ray,  $P_{ij}=1$ ; for K fluorescing L,  $P_{ij}=4.76$ ; for L fluorescing K,  $P_{ij}=0.24$ .

The fluorescence correction thus depends on absorption edge jump-ratio ( $r$ ), the fluorescent yield ( $\omega$ ) of the fluorescer X-ray, mass absorption coefficients, the take-off angle and the operating voltage. To understand the effect of  $\psi$  and  $E_0$  on the fluorescence correction, the Mg-Al binary alloy is again considered. Since  $\text{AlK}\alpha$  ( $E_K=1.487$  keV) is highly absorbed in Mg ( $E_{c(\text{K-shell})}=1.303$  keV) and  $E_K^{\text{AlK}\alpha} > E_{c(\text{K-shell})}^{\text{Mg}}$ ,  $\text{MgK}\alpha$  will be fluoresced. Using the above equations,  $\omega$  from Bambynek et al. (1972),  $(\mu/\rho)$  from Heinrich (1986) and  $E_c$  from Bearden (1964),  $F_{\text{MgK}\alpha}$  in a range of Mg-Al compositions is calculated under different  $\psi$  and  $E_0$  conditions. The plots show that  $F_{\text{MgK}\alpha}$  increases with increasing  $E_0$  and Al-content of the specimen. Changing  $\psi$  does not have a significant effect on the correction. A high  $\psi$  is preferred because it minimizes the absorption correction. Also, the error in the fluorescence correction is low at low  $\psi$  and does not increase at high  $\psi$ . Therefore, a low  $E_0$  and high  $\psi$  angle is recommended.



### 3.1.4. Continuum fluorescence correction

Energy of continuum X-rays range between 0 keV and  $E_0$ . When the energy of the continuum X-rays is greater than the critical excitation energy of an atomic shell of an element in the specimen, the element is fluoresced. Thus, continuum X-rays with energies between  $E_c$  and  $E_0$  cause fluorescence and the fluorescence effect of all energies between  $E_c$  and  $E_0$  must be considered in continuum fluorescence correction. Myklebust et al. (1979) concluded that continuum induced fluorescence may be ignored if  $f(\chi) < 0.95$ ,  $C_i > 0.5$  and  $Z_{std}$  (atomic number) is similar to  $Z_{spec}$ . By choosing a low overvoltage and a high take-off angle continuum fluorescence correction can be avoided except while analyzing a heavy component in a light matrix (e.g., U in a common silicate mineral) when  $f(\chi) > 0.95$ . In such a case, a low energy characteristic X-ray of the element should be analyzed (e.g.,  $\text{UM}\alpha$ ).

### 3.1.5. The $\phi(\rho z)$ correction procedure

The  $\phi(\rho z)$  correction procedure uses experimentally measured depth-distribution of X-rays to model the atomic number and the absorption corrections with a single expression. The equations for generated and emitted X-ray intensities (Eqn. 2.14 and 3.14) are combined:

$$\mathbf{Z}_i \mathbf{A}_i = \frac{\int_0^\infty \phi_i(\rho z) \exp^{-\chi_i \rho z} d(\rho z)}{\int_0^\infty \phi_i^*(\rho z) \exp^{-\chi_i \rho z} d(\rho z)} \quad (3.34)$$

and modeled empirically in terms of  $\alpha$ ,  $\beta$ ,  $\gamma$  and  $\phi_0$  (Packwood and Brown, 1981), or semi-empirically in terms of  $\phi_0$ ,  $R_m$ ,  $R_x$  and the integral of the  $\phi(\rho z)$  distribution (Pouchou and Pichoir, 1984). The fluorescence correction is calculated separately with the Castaing-Reed method (Eqn. 3.26) and combined with Eqn. 3.34 to obtain the full ZAF correction.

## 4. DETECTORS IN THE ELECTRON MICROPROBE

The electron microprobe can be used to obtain high resolution scanned images of the surface of a specimen by rastering the electron beam over an area of the surface. The signal is plotted on the display monitor as the beam scans thus forming a scanning image. Depending on the signal used, an image can be a scanning electron image, an elemental X-ray map or a cathodoluminescence (CL) image. Scanning electron images utilize secondary electrons (SE) or back-scattered electrons (BE). X-ray compositional maps utilize the characteristic X-rays of elements that may be obtained either through the wavelength dispersive spectrometers (WDS) or the energy dispersive spectrometer (EDS). A CL image uses the light signal generated in response to the electron beam.

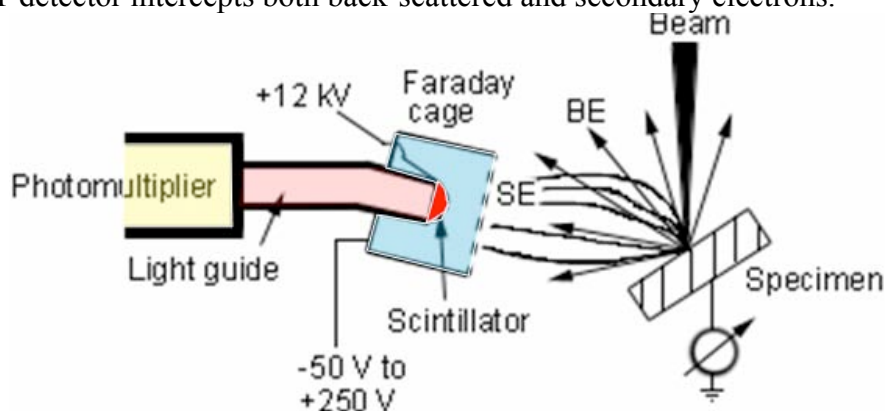
### 4.1. ELECTRON DETECTORS

Back-scattered electrons have energies between 0 keV and  $E_0$ . In contrast, secondary electrons have energies in the range 0-50 eV, mostly between 3 and 5 eV. Therefore, different methods are required for the detection of the two types of electron signal.

#### 4.1.1. Everhart-Thornley (E-T) detector for topographic contrast

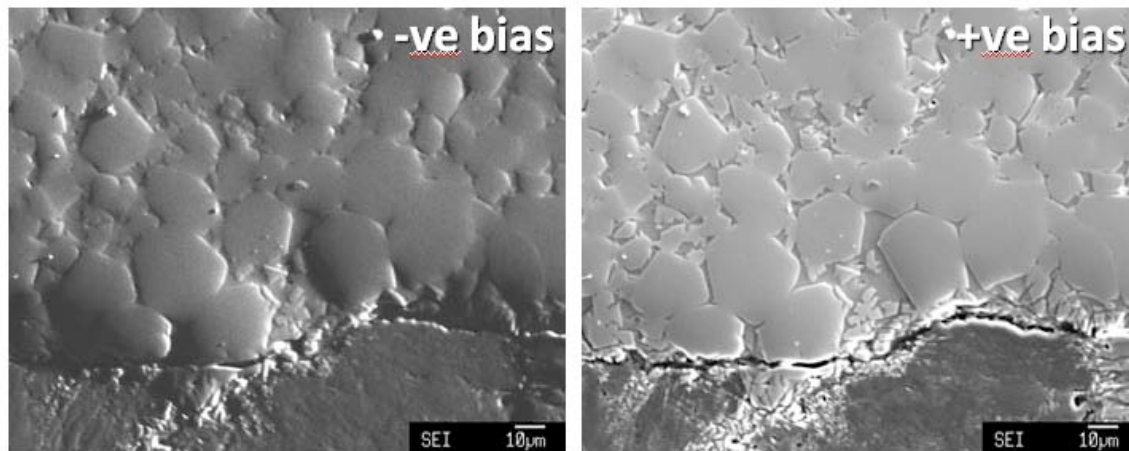
The E-T detector consists of a scintillator maintained at a large positive potential of 10 to 12 kV to attract the incoming electrons. The electrons interact with the scintillator and produce light that travels through a light guide, a solid plastic or glass rod, to a photomultiplier. Light produces electric current in the photomultiplier and the current is amplified by an amplifier.

The scintillator is enclosed in a Faraday cage which can be biased to a negative or positive potential (-50 to +250 V). When the E-T detector is negatively biased, only the high energy back-scattered electrons are able to enter the detector, whereas, a positively biased E-T detector intercepts both back-scattered and secondary electrons.



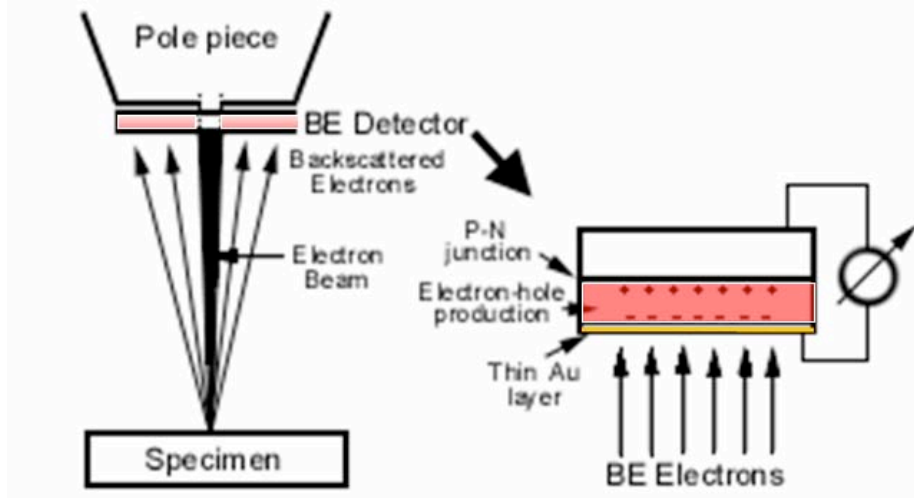
The E-T detector is mounted on one side of the sample chamber receiving a highly directional view of the specimen. As a result, when imaging a fractured surface, the faces directly in the line-of-sight of the detector appear brighter than the other faces. A negatively biased detector rejects the secondary electrons and the faces not in line-of

sight of the detector appear dark producing a shadowing effect. This harsh contrast is reduced when the detector is positively biased because secondary electrons produced on the faces not in line-of-sight are also pulled into the detector. The E-T detector is thus a useful tool for topographic imaging.

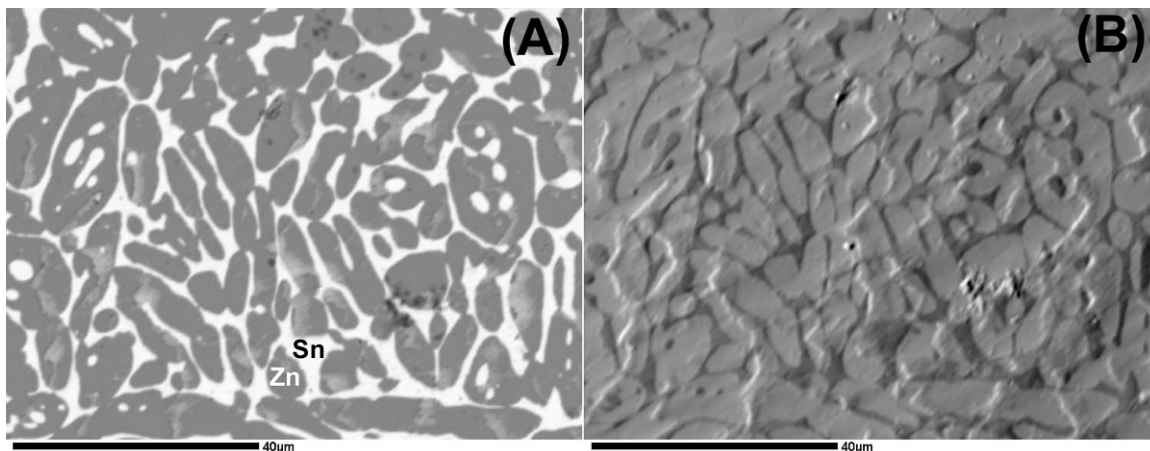


#### 4.1.2. Solid-state diode detector for compositional and topographic contrast

The solid-state diode detector is a semiconductor that tracks changes in voltage in an electrical circuit as a result of electron-hole production in the detector from interactions with back-scattered electrons. It is a flat, annular wafer mounted on the pole-piece of the objective lens directly above the specimen. Low energy electrons such as secondary electrons fail to produce electron-hole pairs in the diode and are not detected.



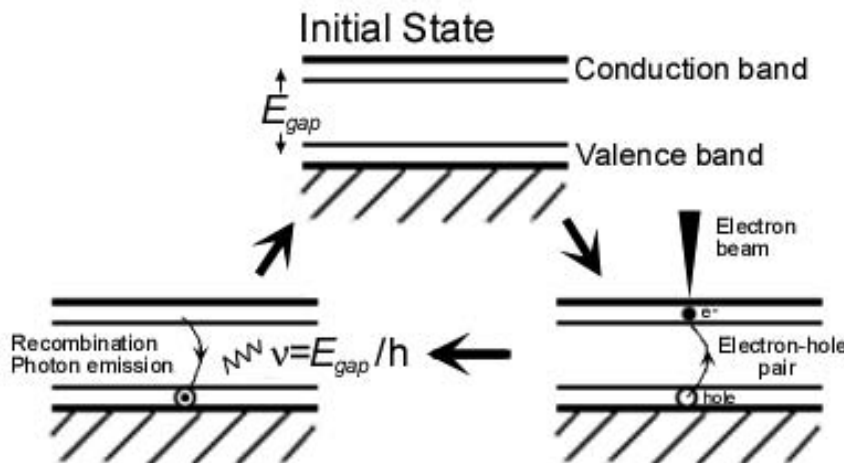
The annular detector is split into two semi-circles, A and B. When signals from both parts are added (A+B mode), good compositional contrast results. The A-B mode is analogous to a stereoscopic view and produces topographic contrast.



Scanning backscattered electron images of a Zn-Sn composite collected through a solid-state diode detector in (A) A+B, or compositional mode; (B) A-B, or topographic mode

## 4.2. CATHODOLUMINESCENCE DETECTOR

When semiconductors interact with energetic electrons, they produce long-wavelength ultraviolet, visible and infrared radiations known as cathodoluminescence (CL). Cathodoluminescent materials have a filled valence band and empty conduction band separated by an energy gap,  $E_{\text{gap}}$ , of forbidden energy states. When an energetic beam electron scatters inelastically, an electron from the valence band may move to the conduction band leaving a hole in the valence band. When the electron and the hole recombine, energy equal to  $E_{\text{gap}}$  is released as a photon. This energy,  $E_{\text{gap}}$ , can be used to identify the specimen by CL spectrometry. Presence of impurity, however, creates additional energy states in the energy gap and changes the wavelength and the intensity of the light. The light signal can thus be used to identify the impurity and obtain a CL image to study the spatial distribution of the impurity.



CL can also be excited by X-rays generated in the sample. Hence, the volume of CL excitation can be larger than the primary electron interaction volume resulting in poorer image spatial resolutions compared to scanning electron images. Thin films usually produce CL images with a better resolution than bulk samples.

A CL spectrometer is attached to the optical microscope port of the electron microprobe. When studying CL, the optical microscope light source is turned off so that the only light coming through the ocular is the light generated by the sample.

### 4.3. X-RAY DETECTORS

An electron microprobe is usually equipped with an energy dispersive spectrometer (EDS) and several wavelength dispersive spectrometers (WDS) for X-ray spectrometry. An X-ray detector is a part of the EDS or WDS.

#### 4.3.1. Energy Dispersive Spectrometer (EDS)

An energy dispersive spectrometer (EDS) takes advantage of the phenomenon of electron-hole production by energetic X-rays in a semiconducting lithium-drifted silicon (Si(Li)) or germanium detector. Electric current produced in the detector is proportional to the incident X-ray energy. A multichannel analyzer (MCA) is used to analyze the electrical pulses and construct an X-ray spectrum for the entire energy range (0 keV to  $E_0$ ) in the form an energy histogram. Elements down to Be ( $Z=4$ ) may be detected with a very thin window or a window-less detector.

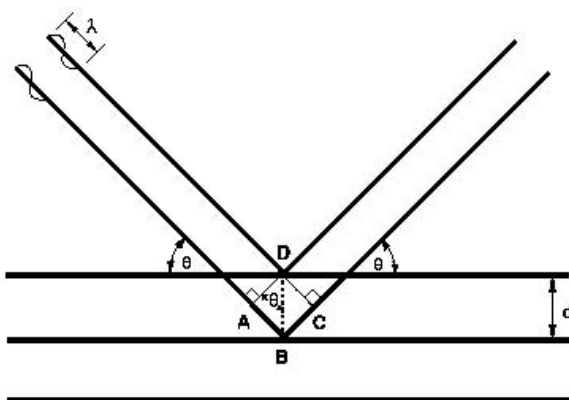
Pure Si is a semiconductor and a good material for a detector. However, Si usually contains some B as impurity that creates holes in the valence band of Si. This electron deficiency makes Si a conductor. Since B is a p-type dopant, an n-type dopant such as Li is added to Si to compensate the electron deficiency created by B. Li is applied on the surface of Si and allowed to diffuse into the crystal. This forms a micrometer-thick p-n zone at the Si-Li interface that acts as an intrinsic semiconductor. Most of the Li is removed from the surface to expose the p-n zone. A reverse bias is applied under liquid nitrogen temperature to the p-n zone, which enlarges the intrinsic zone to a thickness of a few millimeters. Li is mobile under an applied bias at room temperature. Hence, a Si(Li) detector should always be operated at liquid-nitrogen temperatures to prevent damage.

#### 4.3.2. Wavelength Dispersive Spectrometer (WDS)

A WDS system consists of two components: an analyzing crystal and an X-ray detector known as the proportional counter. WDS takes advantage of the Bragg diffracting characteristics of an analyzing crystal to preferentially diffract the wavelength of interest toward the detector. Bragg's law is defined as:

$$n\lambda = 2d \sin \theta \quad (4.1)$$

where,  $\lambda$  is the wavelength of the X-ray,  $d$  is the lattice spacing of the crystal,  $\theta$  is the angle of incidence and diffraction and  $n$  is the order of reflection. X-rays are reinforced after diffraction when the path lengths between two rays differ by an integral ( $n$ ) of the wavelength. Combined reflections from a large number of lattice planes result in a narrow intensity distribution around a peak. For example, the measured full-width half-maximum (FWHM) energy interval of  $\text{MnK}\alpha$  is about 10 eV compared to the natural value of 2 eV.

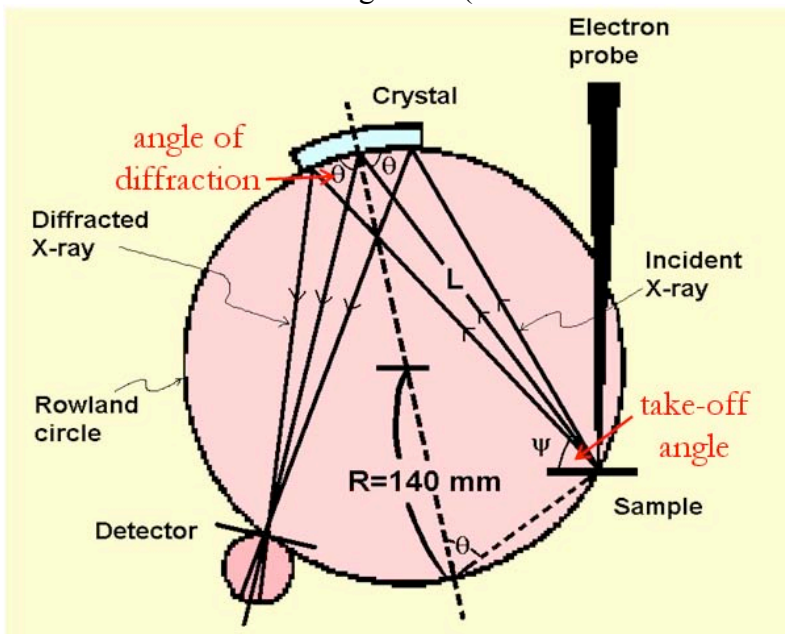


**Diffraction according to Bragg's law. Strong scattering of x-rays of wavelength  $n\lambda$  occurs at angle  $\theta$ . At all other angles, scattering is very weak.**

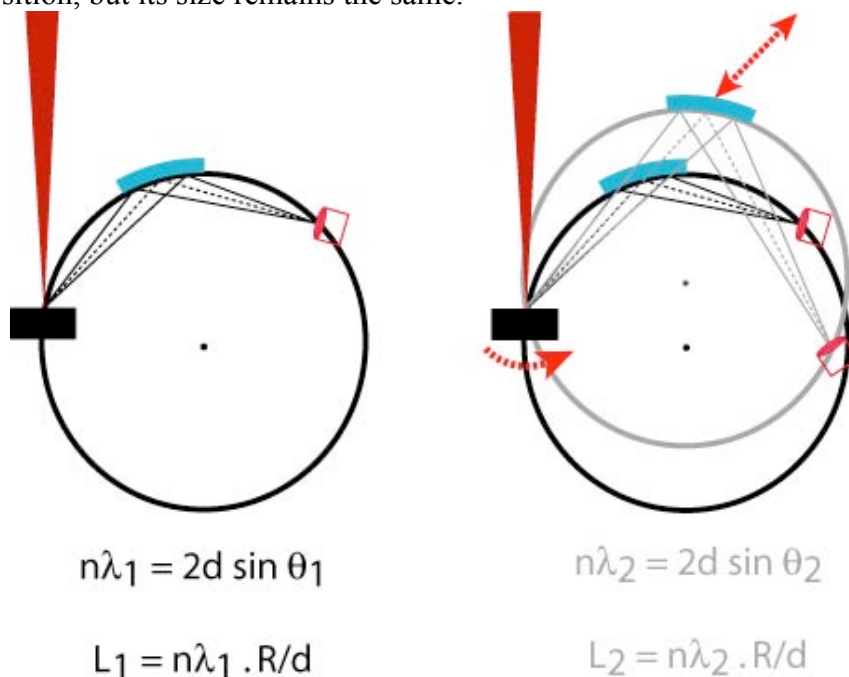
In WDS, the X-ray source (point of the sample from the X-rays are emitted), the analyzing crystal and the detector are positioned on the circumference of a focusing circle known as the Rowland circle. In a Johansson type fully focusing spectrometer, the crystal is curved to a radius of curvature of  $2R$  and then ground to  $R$ , so that its lattice planes and the focusing circle have the same curvature. The diffracted X-rays are thus fully focused into the detector. In practice, crystals are not ground because it degrades the resolution of the crystal. This compromise, known as Johann optics, does not seriously impair the spectrometer resolution. From the geometrical configuration of the instrument,  $\lambda$  is related to  $L$ , the distance between the sample and the analyzing crystal by the following relation:

$$L = n\lambda.R/d \quad (4.2)$$

(mm), where,  $R$  is the radius of the focusing circle (140 mm or 100 mm on JEOL).



To detect different X-ray wavelengths, the crystal is moved in a straight line toward or away from the sample at an angle,  $\psi$  (take-off angle), the angle between the specimen-surface and the X-ray travel direction. The take-off angle is fixed by the design of the instrument. As the crystal moves, it also rotates so that the X-ray incidence angle,  $\theta$ , changes. As a result, different wavelengths are diffracted. The detector moves simultaneously so that it remains in path of the diffracted X-rays. The focusing circle changes position, but its size remains the same.

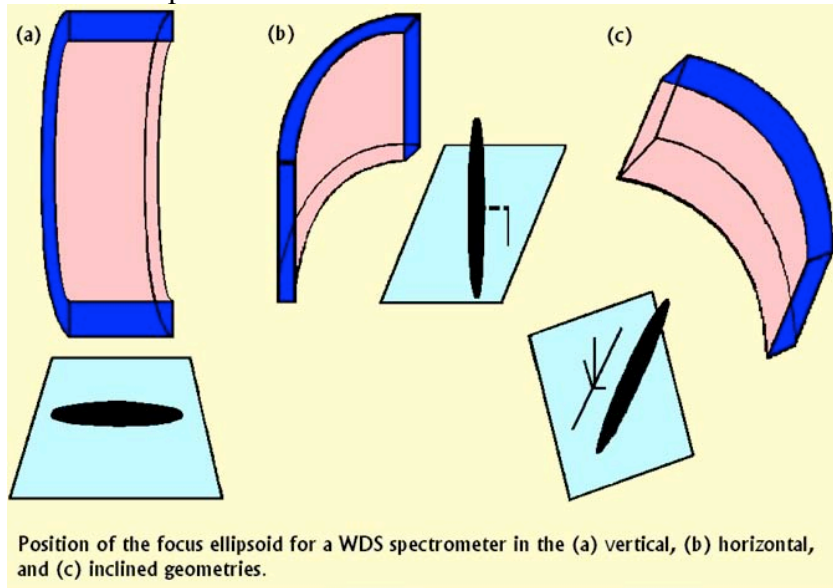


#### 4.3.2.1. *Diffracting crystal in WDS*

Because of the characteristics of WDS, X-rays emitted from only a small elliptical volume of the sample reaches the detector. The shape of this X-ray focus volume depends on the shape of the analyzing crystal and is usually an extremely elongated ellipsoid. The major axis of the focusing ellipsoid is proportional to the width of the diffracting crystal and has a length of several millimeters.

In electron microprobes, WD spectrometers are usually mounted vertically so that the focusing circle is vertical. In this configuration, the major axis of the focusing ellipsoid is horizontal and in the plane of the specimen-surface. A small movement of the specimen in the vertical direction may move the surface outside the focusing ellipsoid and the emitted X-rays will fail to reach the detector. Therefore, the surface is always focused with an optical microscope coaxial with the electron beam during an analytical session. The optical microscope has a shallow focus and the surface can be focused accurately. During routine maintenance, the spectrometer is slowly moved up or down while the surface is in optical focus until the X-ray counts are maximized, ensuring that the major axis of the focusing ellipsoid is on the specimen-surface. At the start of an analytical session, the surface is focused both with the optical microscope and the

objective lens-controls of electron beam. This ensures that the specimen-surface is in X-rays focus when it is in optical focus.



The primary X-ray production volume is much smaller than the volume of the focusing ellipsoid. Since X-ray fluorescence may occur from a much larger volume than the primary X-ray volume, a vertical spectrometer will intercept a significant amount of the fluoresced X-rays. This is a minor problem in a horizontal or inclined spectrometer. However, such configurations require low X-ray take-off angles to maximize the X-ray signal in the detector (e.g., in the horizontal configuration, the Rowland circle is also horizontal). Because of absorption and fluorescence correction issues, low take-off angles are not recommended.

Analyzing crystals available on the JEOL JXA Superprobes at MIT and elements commonly analyzed with them are as follows:

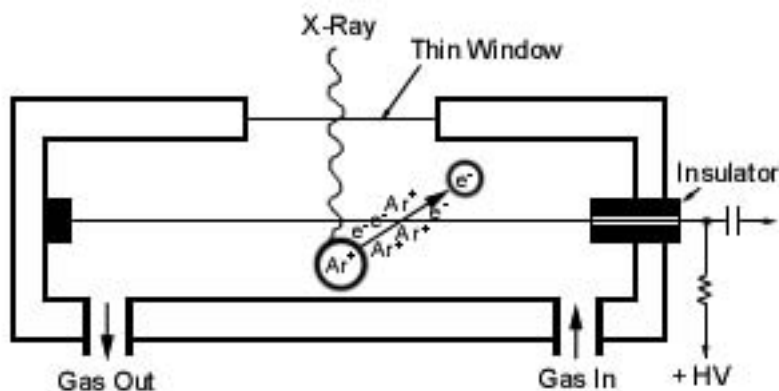
	2d (nm)	Atomic Number										
		6	14	22	30	38	46	54	62	70	78	86
TAP	2.576	8O	15P	24Cr	41Nb	46Pd	79Au					
PET	0.8742	13Al	25Mn	36Kr	65Tb	70Yb						
LIF	0.4027	19K	37Rb	48Cd								

K $\alpha,\beta$ 
L $\alpha,\beta$ 
M $\alpha,\beta,\gamma$

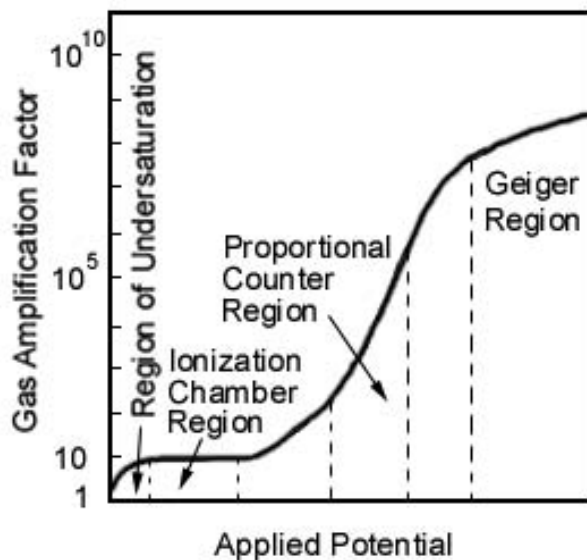
	2d (nm)	Be	B	C	N	O	F
LDE1	Approx. 6			• ••	⊙	⊙	⊙
LDEB	Approx. 14.5	⊙	⊙				
LDE2H	Approx. 10		⊙	⊙			

#### 4.3.2.2. X-ray detector in WDS: proportional counter

The commonly used detector in WDS is known as a proportional counter and consists of a gas filled tube with a thin tungsten wire along the tube-axis maintained at a potential of 1-3 kV. In a flow counter, gas flows through the tube. Sealed counters are also used. X-rays enter the tube through a thin window and ionize the gas atoms. The electron ejected from the gas atom may ionize other gas atoms. The tungsten wire collects the charge and creates a voltage pulse that is amplified and counted by the electronics.

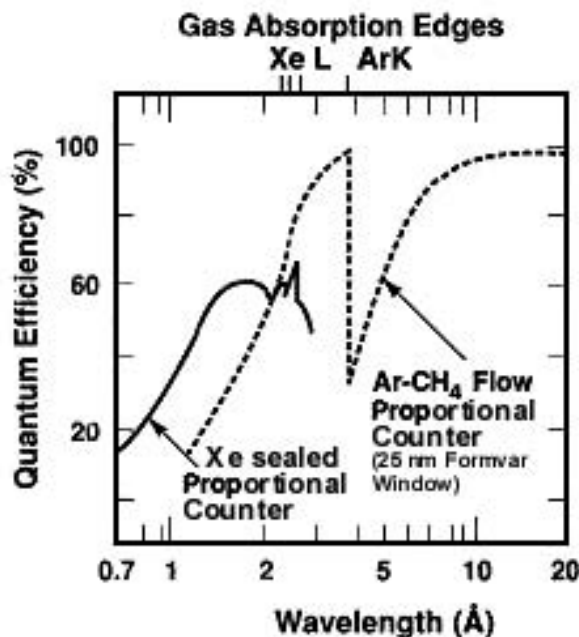


Because one ionization in the gas can set off a chain of ionizations, the signal is amplified internally resulting in count rates of 0-50,000 counts per second. The gas amplification factor, a measure of the internal amplification, varies proportionally to the applied bias in the tungsten wire with a range of voltage known as the proportional counter region.



The type of gas used in the counter depends on the wavelength of the X-ray to be detected. The efficiency of detection, known as the quantum efficiency, of Xe is greater than that of Ar for short wavelength X-rays. Since the LIF and PET crystals are appropriate for short wavelength detection, these crystals are combined with sealed Xe-

counters in WD spectrometers. The thin window on a sealed Xe-counter is made of Be. Ar, diluted with 10% methane (P-10 gas), has a better quantum efficiency for long

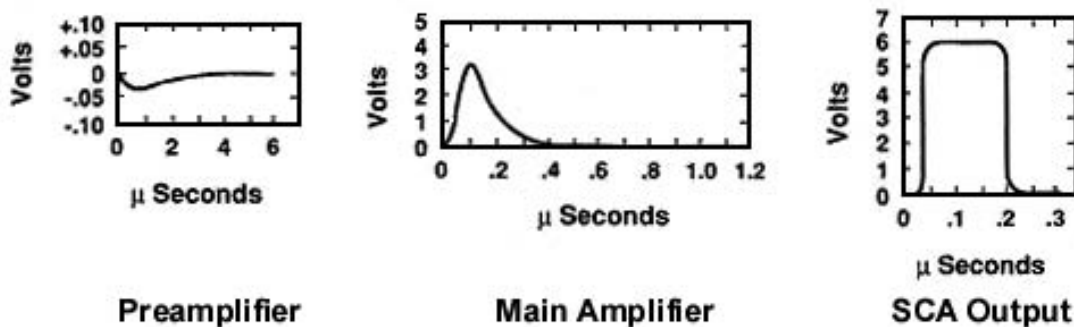


wavelength X-rays. Hence, flow-proportional counters with P-10 is combined with TAP or LDE for light element detection. The window material on a flow Ar-counter is usually an organic compound such as Formvar or cellulose nitrate. The efficiency of an Ar-counter may be improved by increasing the gas pressure to 2-3 atmospheres.

#### 4.3.2.3. Signal processing in WDS: pulse height analysis (PHA)

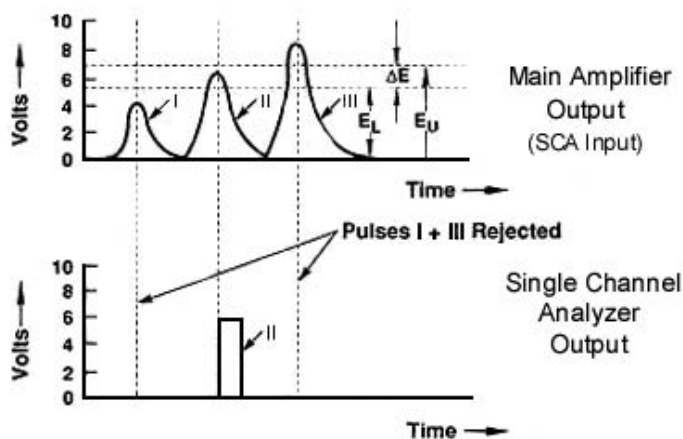
The signal generated in the proportional counter passes through a preamplifier to produce a small negative voltage pulse. In turn, this pulse passes through the main amplifier that inverts, amplifies and shapes the pulse such that its voltage has Gaussian distribution. If the gas amplification factor, the preamplifier and amplifier gains and the capacitance of the preamplifier are constant, the voltage of the amplifier output pulse is directly proportional to the energy of the X-ray that entered the proportional counter.

Output pulses from the amplifier now enter the single channel analyzer (SCA). An SCA selects pulses within a preset voltage range and produces fixed rectangular



Typical WDS x-ray detection pulse shapes

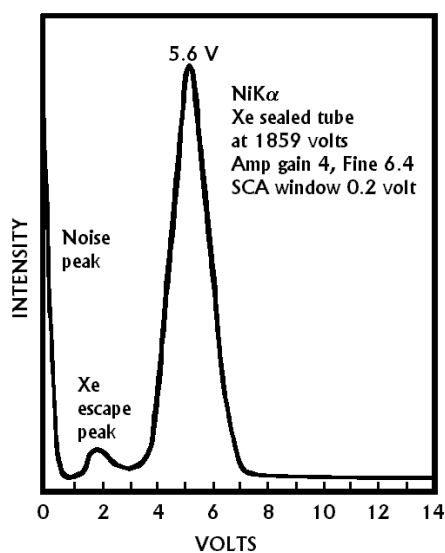
pulses of a fixed voltage and duration compatible with scalar and rate-meter input requirements or the digital counting system. Selection of pulses within a predetermined voltage range is known as pulse-height analysis (PHA). A baseline,  $E_L$ , and a window



### PULSE HEIGHT ANALYSIS

voltage,  $\Delta E$ , are set such that any voltage pulse outside this voltage range is rejected by the SCA. In the example shown in the figure, only pulses between 5 and 7 eV (pulse II) are accepted. The PHA settings may depend on the count rate.

To determine  $E_L$  and  $\Delta E$  an SCA scan is employed. The pulse-voltage distribution is obtained by selecting a small window voltage ( $\Delta E$  of a few tenths of a volt) and slowly moving the baseline over the whole SCA voltage range (0-10 V). A typical SCA scan shows noise near 0 V, an escape peak depending on the detector gas and the actual energy peak. The escape peak corresponds to an energy equal to the actual energy minus the characteristic energy of the detector gas (e.g., 2.96 keV for  $\text{ArK}\alpha$ ). Escape peaks are produced when energy of characteristic X-rays generated in the detector gas (e.g.  $\text{ArK}\alpha$ ) by the X-rays entering the counter leaves the counter. The energy of the X-ray being



Pulse distribution of  $\text{NiK}\alpha$  determined by a single-channel analyzer

measured is diminished by an amount equal to the critical excitation energy for inner-shell ionization of the detector-gas.

PHA is normally used to eliminate the low energy noise. In addition, PHA can also be used to eliminate X-ray energies of interfering elements. This is especially useful when the analyzing crystal is positioned for background measurements. Higher order ( $n > 1$ ) X-rays of transition metals can be efficiently eliminated by optimizing the PHA settings during light element analysis.

The percentage resolution of a proportional counter is the energy width of a peak at FWHM (full-width at half-maximum) divided by the mean peak energy multiplied by 100. A properly functioning counter has Gaussian distribution of pulses and a resolution of between 15 and 20%.

A finite time elapses during which an X-ray pulse processes by the detector system. During this time interval, known as the dead-time, the detector is unavailable to process subsequent pulses. The dead-time corrected count rate is given by  $N/(1-\tau N)$ , where  $N$  is the measured count rate, and  $\tau$  is the dead time. One method of determining  $\tau$  consists of plotting  $N$  versus the beam current. The beam current is proportional to the count rate. A deviation from a straight line on the plot is due to the dead-time, which can be modeled with a polynomial expression.

## 5. COMPOSITIONAL IMAGING BY WDS

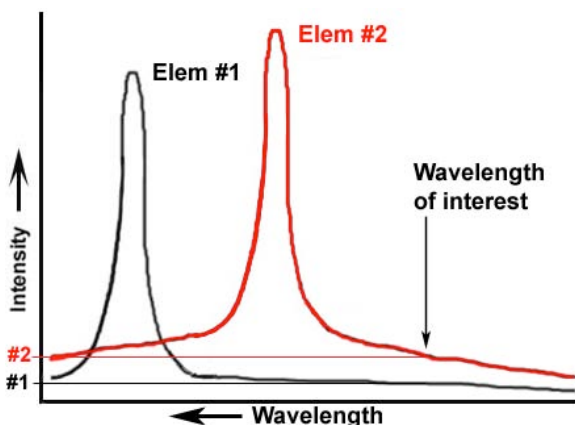
The output from the proportional counter of a WD spectrometer can be used to construct an X-ray image of the sample showing the spatial distribution of an element. Elemental X-ray maps are acquired either by beam-rastering in which the electron beam rasters over the area to be imaged, or by stage-rastering in which the electron beam is stationary while the stage moves. A set of X-ray elemental maps can be used to estimate phase proportions and bulk chemical composition and studying textural relations in a multi-phase composite sample.

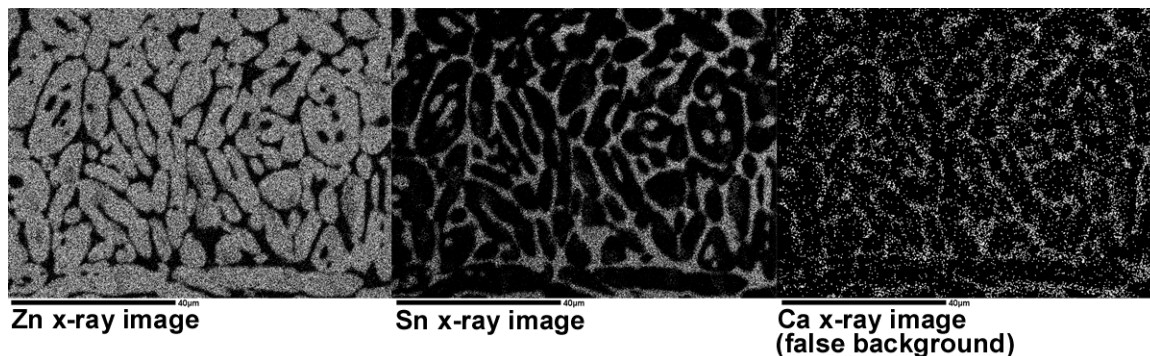
The resolution of an X-ray map depends on the step-size of measurements as the beam moves relative to the sample. Each point measurement corresponds to a pixel on the image. The X-ray signal may be manipulated by setting an appropriate beam current and a dwell-time, the time the beam spends on each point for measurement. The quality of an X-ray map depends on the concentration of the element being mapped and the contrast in the map depends on the difference in concentration of the element in the different phases of the sample. The acquisition time of X-ray maps depends on the stage speed. In addition to the hardware limitations (e.g., stage-motor capability), the stage speed decreases for higher resolutions requiring more number of steps and as the dwell time increases. A 30 mm x 15 mm area may typically be mapped overnight at a resolution of 20  $\mu\text{m}/\text{step}$  and a dwell time of 30 msec/point.

Digital compositional images may provide a complete quantitative analysis at every pixel scanned if the pixel data are corrected for background, divided by standard intensities and corrected for matrix effects. By using several WD spectrometers, the major elements can be mapped simultaneously for matrix corrections. However, because of short dwell-times the chemical composition of each point will be relatively inaccurate. Using long dwell-times may result in unacceptably long acquisition times.

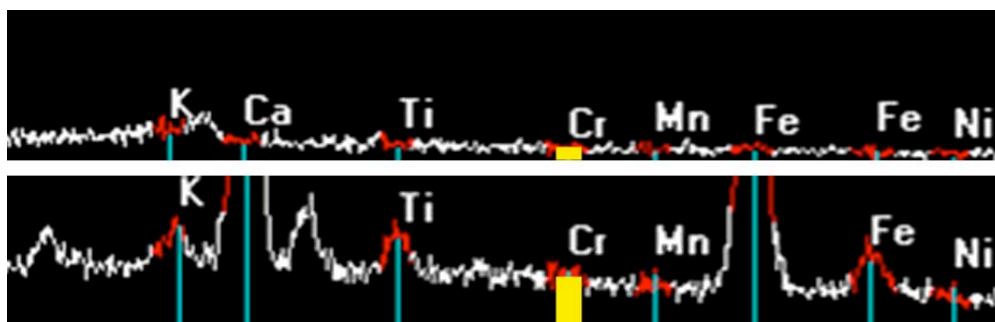
### 5.1. BACKGROUND CORRECTION IN WDS COMPOSITIONAL IMAGING

X-ray maps not corrected for background may contain a continuum artifact. Continuum X-ray intensities generated by phases with different mean atomic numbers may be different. Thus, a spurious image of an element may result even if that element is absent in the sample.





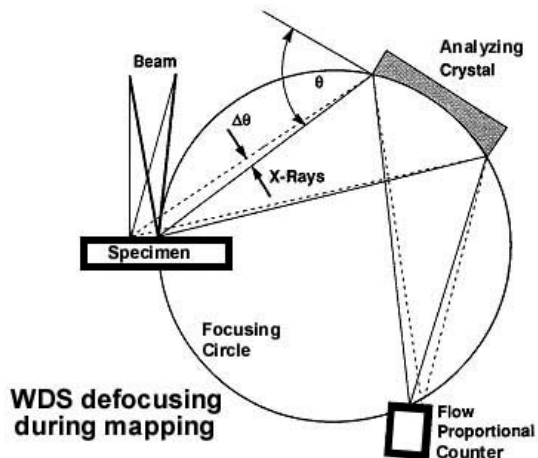
The following example shows spectra of two phases present in the area of the sample being mapped. Cr counts are lower when the beam is on the first phase than when the beam is on the second phase although Cr is not actually present in either phase. The second phase will appear brighter in the map leading to an incorrect interpretation that it contains more Cr.



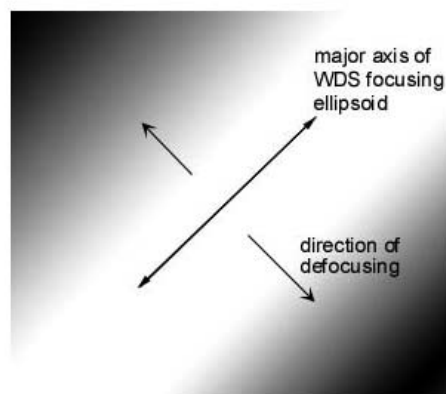
The spurious image may actually serve as a background map that can be used to subtract the background intensity from the elemental maps. However, the background map must be collected with the same spectrometer in a separate session. If many elements are present in the sample, more than one background map be required.

## 5.2. DEFOCUSING IN BEAM-RASTERED WDS X-RAY MAPS

In beam-rastered X-ray mapping, the electron beam may move outside the X-ray focusing ellipsoid of WDS. This will result in an X-ray intensity drop in the areas outside the focusing ellipsoid. The map will show a band of high intensity corresponding to the long axis of the focusing ellipsoid. This defocusing effect is greater at low magnifications because the beam rasters over a large area.



As the beam moves off the optic axis, the displacement in the specimen plane is equivalent to a change in the angle of incidence of the x-rays on the crystal by an angle  $\Delta\theta$ .



Example of a defocused image

There are four approaches to correct WDS defocusing (Newbury et al., 1990):

- *Stage scanning*: Defocusing does not occur in stage-rastered maps because the beam is stationary and vertical during image acquisition.
- *Crystal rocking*: The spectrometer crystal is rocked in synchronism with the beam scan to maintain X-ray focus, i.e., the beam is always incident on the center of the X-ray focusing ellipsoid.
- *Standard mapping*: The specimen and the standard are mapped under the same conditions so that defocusing is identical in both maps. When a k-ratio map is calculated, the defocusing effects cancel out.
- *Peak modeling*: A mathematical expression may be used to correct for the intensity loss in the image.

## 6. QUANTITATIVE ANALYSIS WITH WDS

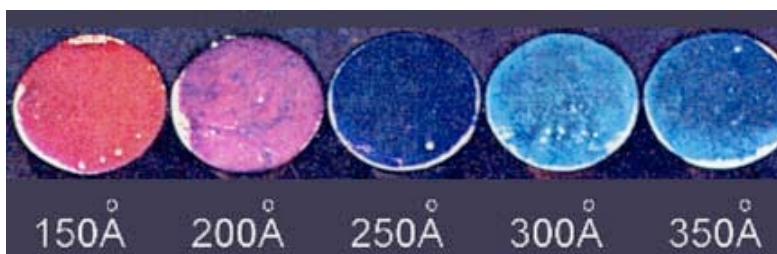
Quantitative analysis with WDS involves careful sample preparation, qualitative identification of elements with EDS, standard intensity measurement (calibration) and measurement of X-ray intensities in the specimen. K-ratios are calculated and the data are reduced through matrix corrections with the quantitative analysis software.

### 6.1. SAMPLE PREPARATION

For qualitative analysis only, the sample may be mounted with double-stick conductive carbon tape on the sample holder. For precise WDS analysis, however, careful sample preparation is essential.

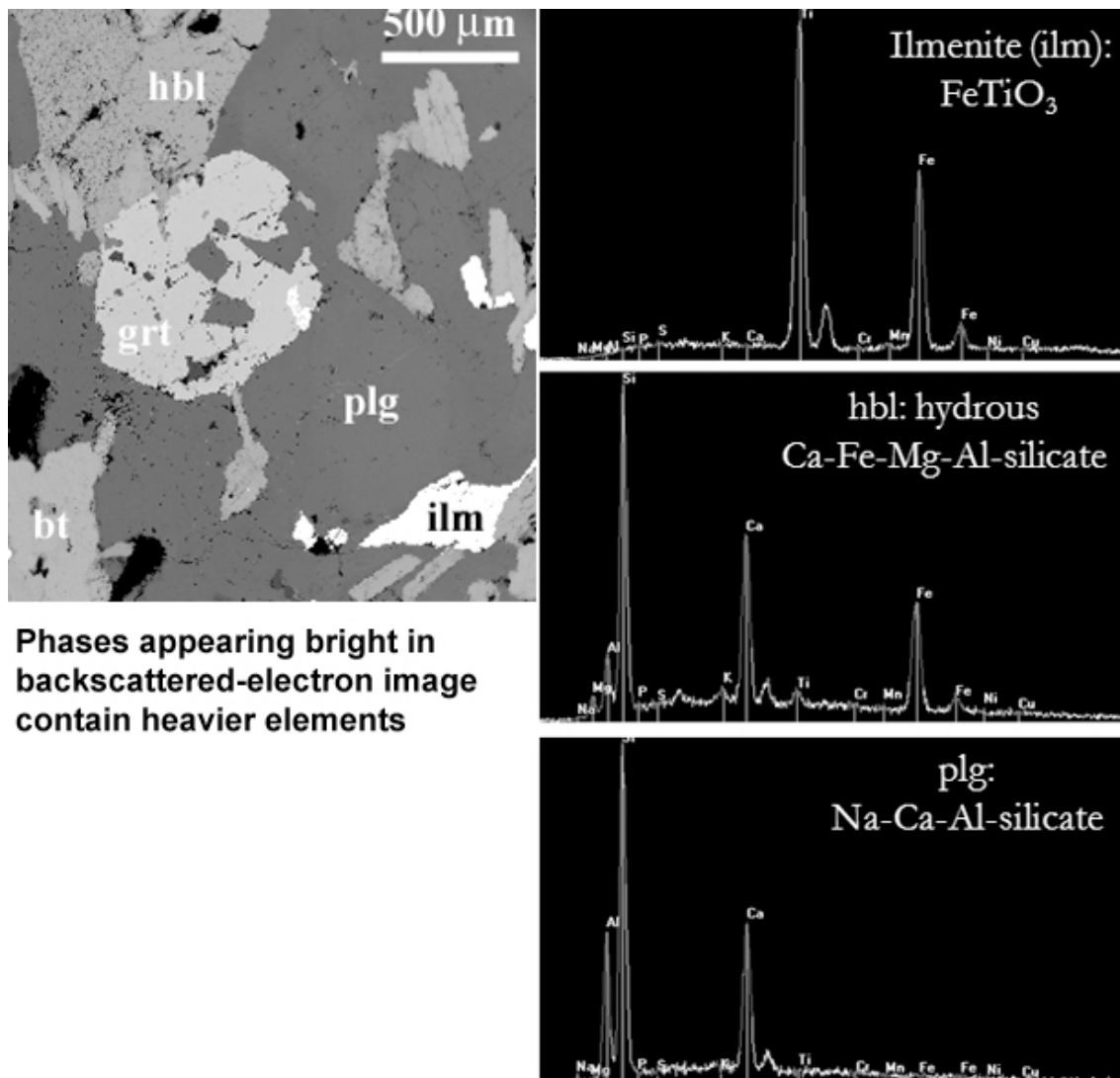
The sample is cut and mounted in epoxy resin in the shape of 0.75" or 1" diameter pellets. The sample mount is then polished first with coarse SiC-paper and then with fine diamond paste or corundum ( $\text{Al}_2\text{O}_3$ ) grit slurry. The final grit size should be at least 0.25  $\mu\text{m}$  and preferable 0.06  $\mu\text{m}$ . For samples that dissolve in water, dry polishing with fine polishing paper is recommended. The polished sample is then washed with clean water in an ultrasonic cleaner to get rid of the polishing grit and other surface dirt. For water soluble samples, this step is avoided. The sample is then dried in air and with blow-duster.

Electrically insulating samples are carbon-coated to ensure conduction of the beam electrons away from the sample. Conductive samples need not be coated. However, if they are mounted in a non-conductive material, carbon-coating is recommended. Furthermore, the standards and the sample should be coated to the same thickness. Carbon coating is carried out by carbon evaporation under vacuum. A polished brass block is used to monitor the thickness of carbon coat deposited on the specimens. As the thickness of coat increases on the brass, it changes color from orange (150 Å) to indigo red (200 Å), blue (250 Å) and bluish green (300 Å). A thickness of about 225 Å is recommended for microprobe analysis at 15-20 kV accelerating voltage.



### 6.2. QUALITATIVE ANALYSIS

Quantitative analysis with WDS requires prior knowledge of which elements are present and to be measured in the sample. Contrast in a back-scattered electron (BE) image corresponds with the major compositional differences among phases in the sample. EDS provides a quick qualitative spectrum. Thus the combination of a BE image and EDS spectra provides a useful tool for quick qualitative analysis.



**Phases appearing bright in backscattered-electron image contain heavier elements**

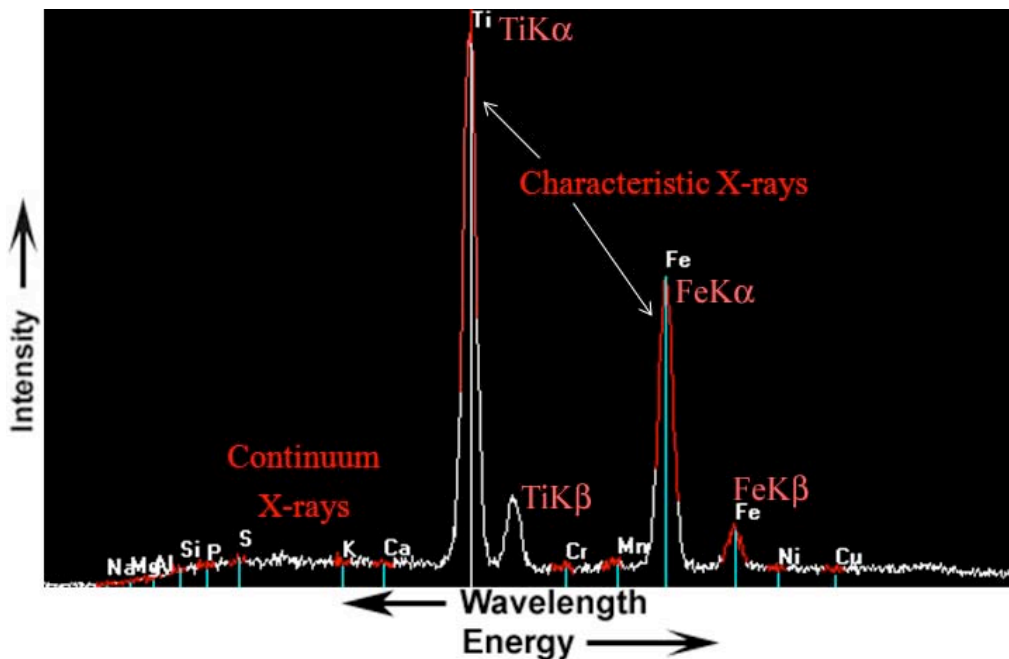
The EDS software includes a KLM marker database that can be used in peak identification. EDS spectra, however, may fail to register trace elements and may contain peak overlaps. Depending on the window material, EDS detects elements only above a certain atomic number. With a Be window, elements above atomic number 9 (F) are detected. Wavelength scans with WDS over a small range of wavelength may be used to qualitatively identify F, O, N, C and B using a light element diffracting pseudo-crystal (e.g., LDE1 or LDEC). WDS scans may also be used to detect trace elements.

### 6.3. CALIBRATION AND UNKNOWN ANALYSIS

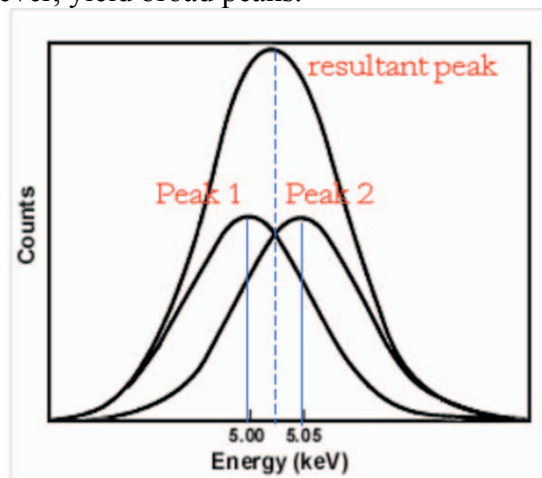
The analytical conditions (e.g., accelerating voltage, beam current, etc.) are set in the beginning and maintained throughout the session. Standard X-ray intensities of the elements to be measured are obtained on appropriately chosen standards. Different standards may be used for different elements. Secondary standards may be analyzed to check if their known compositions are reproduced.

### 6.3.1. Background and Peak Overlap Correction in WDS

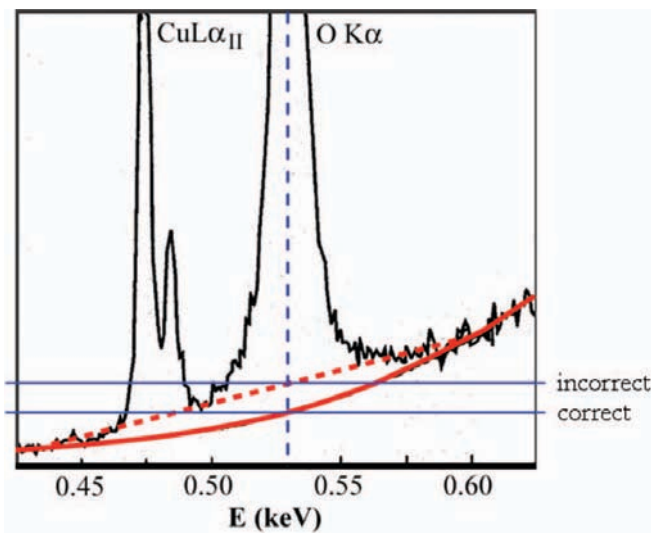
A typical X-ray spectrum acquired through EDS or WDS consists of characteristic X-ray peaks and a background comprised of continuum X-rays. X-ray spectrometry involves measurement of characteristic X-ray peak intensities corrected for background. The usual method to obtain background intensities is by interpolation. The spectrometer is set to measure count rates on two positions, one on each side of the peak, and the background under the peak is calculated by interpolating between the two measurements.



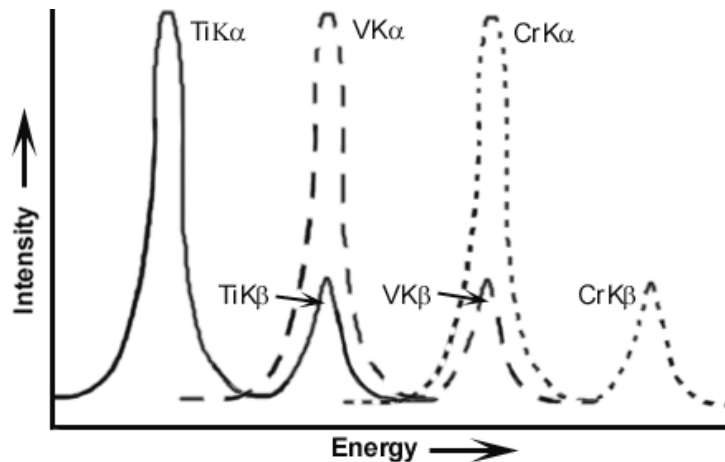
The peaks recorded in an X-ray spectrum are a convolution of the peak from the characteristic X-rays and the instrumental response. In EDS, the peaks are usually broad due to a large instrumental effect. Because of good spectral resolution in WDS, the tall and narrow shape of the peaks are retained. Layered synthetic microstructures (e.g., LDE1 or LDEC), however, yield broad peaks.



Measured X-ray intensities must also be free of peak overlaps. Care must be taken to avoid interfering peaks of other elements both on the peak and the background positions. When a peak is broad, an overlap between adjacent peaks is possible. Even in the case of partial overlaps, the tails of two adjacent peak may overlap. When broad overlapping peaks are present in the spectrum, background modeling using a polynomial fit may be more appropriate.



In case of unavoidable peak overlaps, the magnitude of an overlap can be calculated by measuring the intensity of the overlapping peak on a standard that contains the interfering element, but not the element of interest. For example, in the Ti-V-Cr system, there are two peak overlaps. The  $\text{VK}\alpha$  and the  $\text{CrK}\alpha$  peaks are overlapped by the  $\text{TiK}\beta$  and  $\text{VK}\beta$  peaks, respectively. The intensity contributions from the  $\text{TiK}\beta$  and  $\text{VK}\beta$  peaks must be subtracted from the measured intensities of  $\text{VK}\alpha$  and  $\text{CrK}\alpha$  in order to obtain their true intensities. Following is a schematic representation of the X-ray spectrum of a Ti-V-Cr alloy showing the peak overlaps:



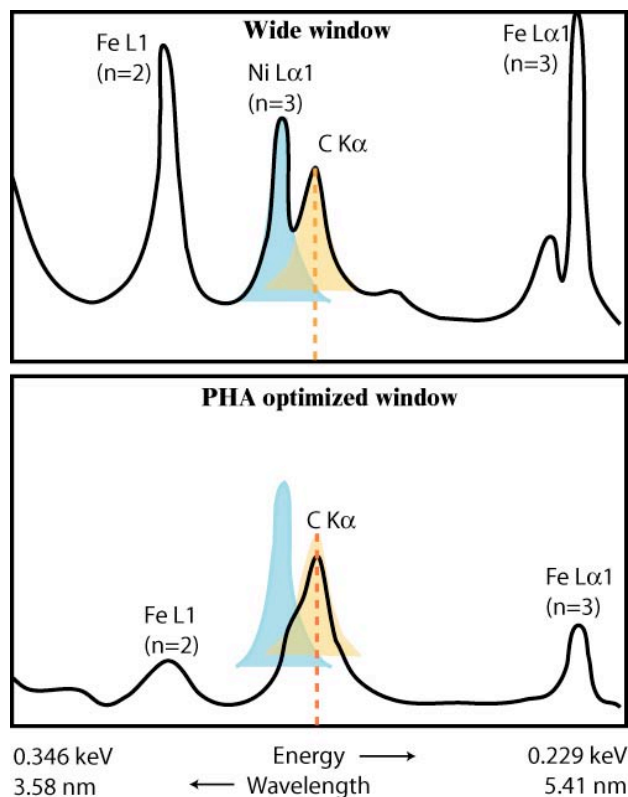
The intensities of the  $\text{VK}\alpha$  and the  $\text{CrK}\alpha$  may be corrected with to the following equations:

$$I_{VK\alpha}^{\text{corr}} = I_{VK\alpha}^{\text{meas}} - \frac{I_{TiK\alpha}^{\text{meas}}}{I_{Ti\text{-std}}} I_{VK\alpha}^{\text{Ti-std}} \quad (6.1)$$

$$I_{CrK\alpha}^{\text{corr}} = I_{CrK\alpha}^{\text{meas}} - \frac{I_{VK\alpha}^{\text{corr}}}{I_{V\text{-std}}} I_{CrK\alpha}^{\text{V-std}} \quad (6.2)$$

where,  $I$  is intensity, "corr" is corrected, "meas" is measured and "std" is standard. To correct the intensity of  $VK\alpha$ ,  $I_{VK\alpha}^{\text{Ti-std}}$  is measured on pure Ti. Since pure Ti does not contain V, the  $I_{VK\alpha}^{\text{Ti-std}}$  measured is because of the presence of  $TiK\beta$ .  $I_{VK\alpha}^{\text{Ti-std}}$  is subtracted from  $I_{VK\alpha}^{\text{meas}}$  measured in the sample after multiplying it with the k-ratio of  $TiK\alpha$  ( $=I_{TiK\alpha}^{\text{meas}} / I_{TiK\alpha}^{\text{Ti-std}}$ ) in the sample, which serves as a scaling factor. The correction for  $CrK\alpha$  is similar, except  $I_{VK\alpha}^{\text{corr}}$  is used in Eqn. 6.2 instead of  $I_{VK\alpha}^{\text{meas}}$ .

The transition metals Ti, V, Cr, Mn, Fe, Co and Ni, and the metals Zr, Nb and Mo emit X-rays at wavelengths similar to the characteristic wavelengths of the light elements such as F, O, N, C and B. The elements Zr, Nb and Mo also have absorption edges, which greatly diminish the emitted intensities of the light elements. For example, the  $NK\alpha$  (31.6 Å) is severely overlapped by  $TiL1$  (31.4 Å). It is thus extremely difficult to measure N in the presence of Ti, specially if N is present in trace amounts. Correctly setting the PHA baseline and window may filter out the higher order X-ray wavelengths. This is demonstrated in the following wavelength scans, in which the higher order lines of Fe and Ni are efficiently subdued and the background lowered with optimal PHA settings for carbon  $K\alpha$ :



## 7. REFERENCES

- Anderson, C.A. and Hasler, M.F. (1966) In *Proc. 4<sup>th</sup> Intl. Conf. On X-ray Optics and Microanalysis* (R. Castaing, P. Deschamps and J. Philibert, eds.) Hermann: Paris, p. 310.
- Bambynek, W., Crasemann, B., Fink, R.W., Freund, H.U., Mark, H., Swift, S.D., Price, R.E. and Rao, P.V. (1972) *Rev. Mod. Phys.*, 44, 716.
- Bearden, J.A. (1964) "X-ray Wavelengths", Report NYO 10586, U.S. Atomic Energy Commission, Oak Ridge, Tennessee.
- Bence, A.E. and Albee, A. (1968) *J. Geol.*, 76, 382.
- Berger, M.J. and Seltzer, S.M. (1964) *Nat. Acad. Sci./Nat. Res. Council Publ.* 1133, Washington, 205.
- Bethe, H. (1933) In *Handbook of Physics*. Springer: Berlin, 24, 273.
- Castaing, R. (1951) Ph.D. Thesis, University of Paris.
- Duncumb, P. and Reed, S.J.B. (1968) In *Quantitative Electron Probe Microanalysis* (K.F.J. Heinrich, ed.), Nat. Bureau Stand. Spl. Publ. 298, 133.
- Duncumb, P. and Shields, P.K. (1966) In *The Electron Microprobe* (T.D. McKinley, K.F.J. Heinrich and D.B. Wittry, eds.), Wiley: New York, p. 284.
- Heinrich, K.F.J. (1969) National Bureau of Standards, Technical Note 521.
- Heinrich, K.F.J. (1986) In *Proc. 11th Intl. Conf. on X-ray Optics and Microanalysis* (J.D. Brown and R.H. Packwood, eds.), Univ. Western Ontario, London, Ont. Canada, p. 67.
- Kanaya, K. and Okayama, S. (1972) *J. Phys. D.: Appl. Phys.*, 5, 43.
- Myklebust, R.L., Fiori, C.E. and Heinrich, K.F.J. (1979) *Nat. Bureau Stand. Tech. Note* 1106.
- Newbury, D.E., Fiori, C.E., Marinenko, R.B., Myklebust, R.L., Swyt, C.R. and Bright, D.S. (1990) *Anal. Chem.*, 62, 1159A and 1245A.
- Packwood, R.H. and Brown, J.D. (1981) *X-ray Spectrom.*, 10, 138.
- Philibert, J. (1963) In *Proc. 34th Intl. Symp. X-ray Optics and X-ray Microanalysis, Stanford University* (H.H. Pattee, V.E. Cosslett and A. Engstrom, eds.) Academic Press: New York, p. 379.
- Pouchou, J.L. and Pichoir, F. (1984) *Rech. Aerosp.*, 3, 13.
- Reed, S.J.B. (1965) *Br. J. Appl. Phys.*, 16, 913.
- Shimizu, R., Kataoka, Y., Ikuta, T., Koshikawa, T. and Hashimoto, H. (1976) *J. Phys. D.: Appl. Phys.*, 9, 101.
- Thomas, P.M. (1964) U.K. Atomic Energy Auth. Rept. AERE-R 4593.
- Yakowitz, H., Myklebust, R.L. and Heinrich, K.F.J. (1973) *Nat. Bureau Stand. Tech. Note* 796.

### 7.1 SOURCES AND RECOMMENDED READING

- 1) Goldstein, J.I., Newbury, D.E., Joy, D.C., Lyman, C.E., Echlin, P., Lifshin, E., Sawyer, L. and Michael, J.R. (2003) *Scanning Electron Microscopy and X-ray Microanalysis* (Third Edition). Kluwer Academic/Plenum Publishers: New York.
- 3) JEOL technical manuals.

## 7.2 ACKNOWLEDGEMENTS

The second edition of the text book by Goldstein et al. (item 1 in above list) was extensively used in preparing these notes. Some of the figures are from this book, but have been altered to suit the needs of this course. A few of the figures are modified from figures in the JEOL technical manuals.

MIT OpenCourseWare  
<http://ocw.mit.edu>

12.141 Electron Microprobe Analysis  
January (IAP) 2012

For information about citing these materials or our Terms of Use, visit: <http://ocw.mit.edu/terms>.